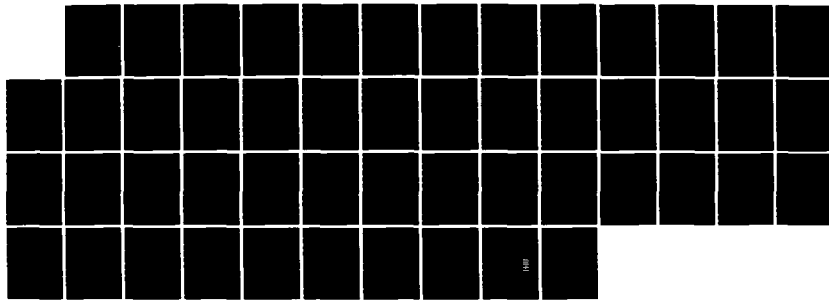
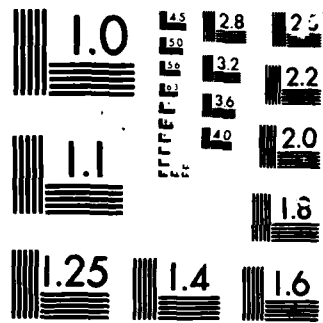


RD-A167 299 A TWO-DIMENSIONAL STUDY OF THE INFLUENCE ON TARGET 5/1  
LOADING OF NUMERICAL M. (U) ARMY BALLISTIC RESEARCH LAB  
ABERDEEN PROVING GROUND MD R E LOTTERO ET AL MAR 86  
UNCLASSIFIED BRL-MR-3503 F/G 20/4 NL





MICROCOPI

CHART

(12)

AD-A167 299

AD



US ARMY  
MATERIEL  
COMMAND

MEMORANDUM REPORT BRL-MR-3503

A TWO-DIMENSIONAL STUDY OF THE  
INFLUENCE ON TARGET LOADING OF  
NUMERICAL WAVE REFLECTIONS FROM  
TRANSMISSIVE COMPUTATIONAL BOUNDARIES

Richard E. Lottero  
John D. Wortman

March 1986

DTIC FILE COPY

APPROVED FOR PUBLIC RELEASE; DISTRIBUTION UNLIMITED.

DTIC  
ELECTED  
APR 29 1986  
S D  
P E

US ARMY BALLISTIC RESEARCH LABORATORY  
ABERDEEN PROVING GROUND, MARYLAND

36-4-29, 010

Destroy this report when it is no longer needed.  
Do not return it to the originator.

Additional copies of this report may be obtained  
from the National Technical Information Service,  
U. S. Department of Commerce, Springfield, Virginia  
22161.

The findings in this report are not to be construed as an official  
Department of the Army position, unless so designated by other  
authorized documents.

The use of trade names or manufacturers' names in this report  
does not constitute indorsement of any commercial product.

UNCLASSIFIED

SECURITY CLASSIFICATION OF THIS PAGE (When Data Entered)

UNCLASSIFIED

SECURITY CLASSIFICATION OF THIS PAGE(When Data Entered)

20. Abstract (cont)

computational grid by generating aggregates of rigid, immobile, and impermeable flow-field cells. The simple transmissive boundaries in HULL simulate a zero-gradient condition across the boundary for both the pressure and the normal component of velocity. Simple transmissive boundaries such as these will partially reflect waves that strike them, including shock, compression, and expansion waves. The strength of these reflected waves is directly related to the strength of the incident waves. These reflected waves then travel back into the computational grid, modifying the flow-field conditions in the regions through which they pass, thereby ending the simulation of free-field conditions. The usual procedure is to locate the transmissive boundaries far enough away from the target so that these artificial waves do not arrive at the target during the time of interest. However, limitations due to available computer storage, cost, speed, or any combination thereof, may necessitate a computational grid design such that some disturbances at the target from the transmissive boundaries are probable. Hence it is necessary to estimate the effects of these disturbances on the computed loading of the target. The analysis of the computations performed here provides insight into the nature of the disturbances and a means for estimating the deviation from free-field results.

UNCLASSIFIED

SECURITY CLASSIFICATION OF THIS PAGE(When Data Entered)

## TABLE OF CONTENTS

	Page
LIST OF ILLUSTRATIONS . . . . .	5
LIST OF TABLES . . . . .	7
I. INTRODUCTION . . . . .	9
II. TARGET . . . . .	9
III. SIMULATED CONDITIONS . . . . .	11
IV. HYDROCODE COMPUTATIONS . . . . .	12
A. General Information . . . . .	12
B. Transmissive Boundary Check. . . . .	12
C. Extended Boundary Reference Computation SS/EB5 . . . . .	27
D. Cross-Check of Computations . . . . .	31
V. CONCLUSION . . . . .	39
REFERENCES . . . . .	41
DISTRIBUTION LIST . . . . .	43

Accession For	
NTIS GRA&I	
DTIC TAB	
Unannounced	
Justification	
By _____	
Distribution/ _____	
Availability Codes	
Dist	Avail and/or Special
A-1	



## LIST OF ILLUSTRATIONS

Figure	Page
1. The Nominal Target Cross-section . . . . .	10
2. Boundary Check Computations for Average Overpressure on the Front Face . . . . .	19
3. Boundary Check Computations for Average Overpressure on the Front Slope . . . . .	21
4. Boundary Check Computations for Average Overpressure on the Top Flat Section . . . . .	23
5. Boundary Check Computations for Average Overpressure on the Back Slope . . . . .	25
6. Boundary Check Computations for Average Overpressure on the Back Face . . . . .	26
7. Vortex Growth Behind the Back Face	
(a) 10 ms. . . . .	28
(b) 20 ms. . . . .	28
(c) 30 ms. . . . .	28
(d) 40 ms. . . . .	28
(e) 43 ms. . . . .	29
(f) 46 ms. . . . .	29
(g) 50 ms. . . . .	29
(h) 610.1 ms . . . . .	29
8. Corrected versus Uncorrected Drag Coefficient for SS/EB5 . . . . .	30
9. Comparison Computations for Average Overpressure on the Front Face .	33
10. Comparison Computations for Average Overpressure on the Front Slope.	34
11. Comparison Computations for Average Overpressure on the Top Flat Section . . . . .	35
12. Comparison Computations for Average Overpressure on the Back Slope .	36
13. Comparison Computations for Average Overpressure on the Back Face .	37
14. Comparison Computations for Drag Coefficient . . . . .	38

**LIST OF TABLES**

<b>Table</b>		<b>Page</b>
1. Hydrocode Computations . . . . .		14
2. Predicted Arrival Times of Artificial Waves from Boundaries. . . . .		18
3. First Deviation from SS/TB5. . . . .		20
4. First Deviation from SS/EB5 (Reference). . . . .		20

## I. INTRODUCTION

One of the principal uses of the US Army Ballistic Research Laboratory (BRL) version of the HULL<sup>1,2</sup> hydrocode has been to perform blast loading computations on military targets. The three-dimensional (3-D) version of HULL has been shown to give excellent agreement with experimental results for

diffraction loading on a box-like target for a weak shock at obliquity<sup>3</sup>. However, that study was carried only through the shock diffraction phase.

More recent studies<sup>4</sup> have been carried out using the cylindrically symmetric version of the HULL hydrocode, with variation axially and radially but not rotationally. The target used in those studies was a rigid, right-circular cylinder, located coaxially within a computational flow field simulating a cylindrical shock tube. Computations were carried out for non-decaying (step) shocks of three different strengths for several shock crossing times so as to estimate the effect of shock tube blockage on drag phase loading. In these computations, the outer-radial boundaries of the shock tube were perfectly-reflecting in order to simulate the interaction of wave reflections between the target and shock tube walls. This work was ended in another computational

study<sup>5</sup> and a combined computational and experimental study<sup>6</sup>.

The conditions for a reflective boundary are reasonably well-defined by creating mirror images in virtual cells beyond the active flow field. The pressure in the virtual cell is set equal to that of the adjacent flow-field cell, and the normal component of velocity is set equal in magnitude and opposite in sign. The simple transmissive boundaries in HULL simulate a zero-gradient condition across the boundary for both the pressure and the normal component of velocity. Simple transmissive boundaries such as these will partially reflect waves that strike them, including shock, compression, and expansion waves. These waves typically reflect in kind from these transmissive boundaries, with their strength directly related to the strength of the incident waves. These reflected waves then travel back into the computational grid, modifying the flow-field conditions in the regions through which they pass, thereby ending the simulation of free-field conditions. The usual procedure is to locate the transmissive boundaries far enough away from the target so that these artificial waves do not arrive at the target during the time of interest. However, limitations due to available computer storage, cost, speed, or any combination thereof, may necessitate a computational grid design such that some disturbances at the target from the transmissive boundaries are probable. This report presents the results from a systematic study of boundary effects for a 2-D target of modest complexity struck by a strong, non-decaying shock wave.

## II. TARGET

The nominal target used in this study, shown in Figure 1, is two-dimensional and has a "barn-like" cross-section. It has a height of 1.83 m (6.0 ft) and a depth (in the direction of shock travel) of 3.05 m (10.0 ft). The top face of the target has front and back sloping sections, each at an angle of 30 degrees to the horizontal, and a central flat section. The vertical sections of the front and back faces are each 1.22 m (4.0 ft) high. There are two variations on this target. The first, hereinafter referred to

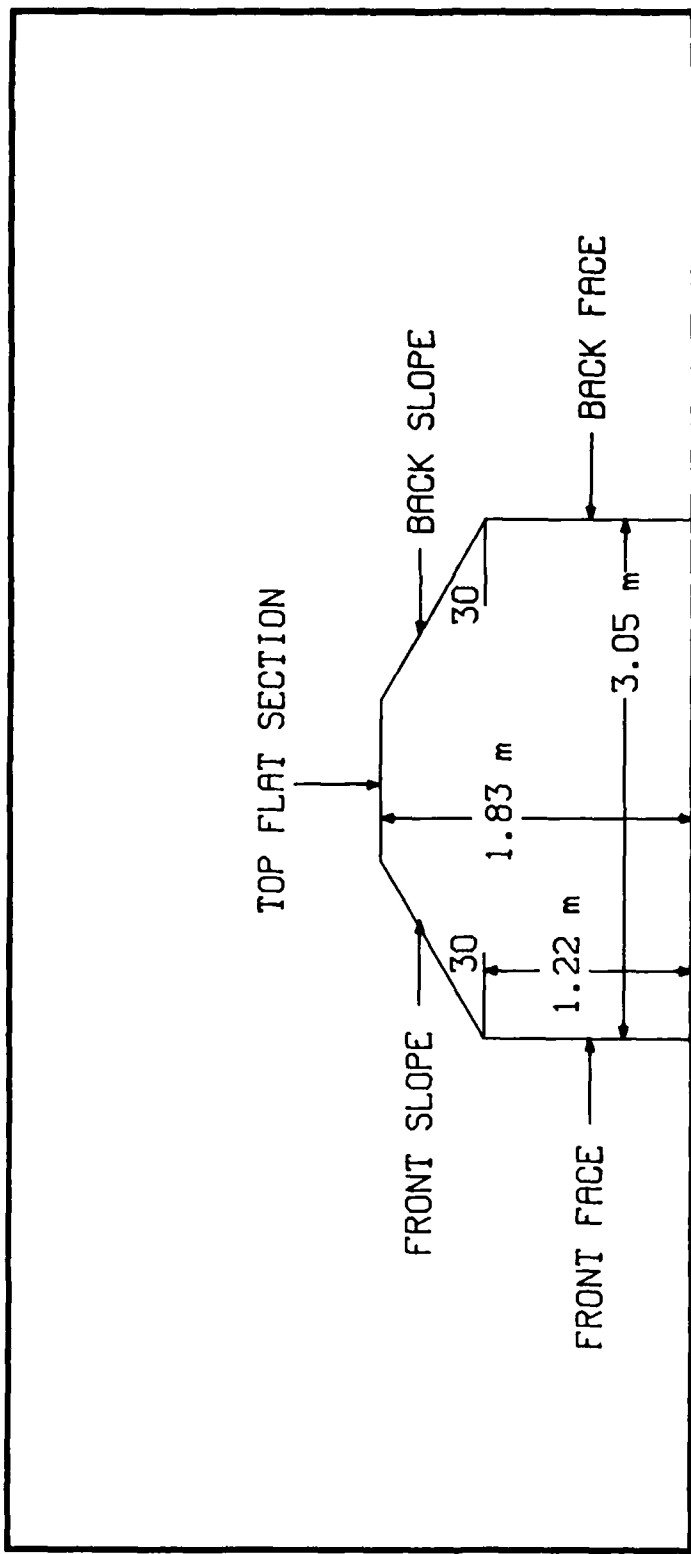


Figure 1. The Nominal Target Cross-section.

as target SS (for Stair-Stepped); uses only fully rigid (island) cells to construct the target, so the front and back slopes for the top face actually resemble "stair-steps." The second, hereinafter referred to as target RT (for Ramped Target), uses combinations of island cells and half-rigid, half-hydrodynamic (shore) cells<sup>2</sup> to construct the target. Most of the computations were done using target SS because the shore cells are available only in 2-D HULL and they cause the code to run somewhat slower. The computations for target RT were done to provide an indication of the effect of using the shore cells to simulate a smooth ramp as opposed to using a stepped approximation. A reference computation that was hydrodynamically two-dimensional was performed for target SS using the 3-D HULL coding. In this way, information gained from the 2-D study can be linked to similar 3-D computations. For the remainder of this report, "front face" refers to the vertical section of the front of either SS or RT, "back face" to the vertical section of the back, "front slope" to the sloping section of the top face, "back slope" to the back sloping section of the top face, and "top flat section" to the flat section in the center of the top face (see Figure 1).

### III. SIMULATED CONDITIONS

The ambient conditions were chosen to be characteristic of those found at the White Sands Missile Range. The ambient conditions were:

static pressure = 85.5 kPa (12.4 psi),  
static density = 0.999 kg/m<sup>3</sup> (0.0624 lbm/ft<sup>3</sup>),  
static temperature = 298.15 Kelvins (536.7 degrees Rankine),  
local sound speed = 346.1 m/s (1136 ft/s).

The blast wave considered is from a 206.8 kPa (30 psi) overpressure step shock. The shocked-gas conditions were:

static pressure = 292.3 kPa (42.4 psi),  
static density = 2.282 kg/m<sup>3</sup> (0.1425 lbm/ft<sup>3</sup>),  
static temperature = 446.3 Kelvins (803.4 degrees Rankine),  
local sound speed = 423.5 m/s (1390 ft/s),  
local Mach number = 0.806,  
dynamic pressure = 132.8 kPa (19.26 psi),  
shock speed = 606.9 m/s (1991 ft/s),  
shock Mach number = 1.753,  
gas velocity = 341.2 m/s (1119 ft/s).

The theoretical conditions on the target front vertical wall for normal reflection were:

static pressure = 817.9 kPa (118.6 psi),  
static overpressure = 732.4 kPa (106.2 psi),  
static density = 4.613 kg/m<sup>3</sup> (0.2880 lbm/ft<sup>3</sup>),  
static temperature = 617.6 Kelvins (1112 degrees Rankine),  
local sound speed = 498.2 m/s (1634 ft/s),  
shock speed 675.1 m/s (2215 ft/s).

#### IV. HYDROCODE COMPUTATIONS

##### A. General Information.

The computations were performed on the BRL's CDC 7600 using the BRL version<sup>1,2</sup> of the HULL hydrocode, a modified version of one obtained from the US Air Force Weapons Laboratory in 1978. The code solves the inviscid Euler equations, using an explicit time step finite difference algorithm (essentially a modified Lax-Wendroff computing scheme). Three series of two-dimensional computations were performed for this study. The first set was performed as a specific check on the influence of artificially reflected waves from the top transmissive boundary on the loading of target SS. The second set of computations, one of which is discussed here, showed the influence of the positions of the upstream and downstream transmissive boundaries on the loading on target SS. The final set was done as a reference set to show the effects of using smooth slopes (target RT) versus stair-stepped slopes (target SS) on the computed loading of the nominal target. This final set also included a hydrodynamically 2-D computation using the 3-D coding to provide a check on the internal consistency within HULL, as the 2-D and 3-D coding have some differences between them. All times quoted in these studies have a reference value of zero for the theoretical arrival of the incident shock at the front face of the target.

All computations were performed with the bottom boundary of the grid defined as a perfect reflector, with no possibility of flow through it. The upstream boundary was defined as a constant inflow boundary, with input flow conditions equal to those for the steady 206.8 kPa overpressure shock defined in the previous section. Any wave, real or artificial, arriving at this boundary does not directly affect the fixed boundary conditions there, but will typically reflect some manner of artificial wave back into the computational grid. Hence, any reference in the following text to artificial waves originating from this boundary should be construed as originating from the region immediately downstream from this boundary. The top and downstream boundaries are simple transmissive boundaries designed to make a zero-gradient match to local flow conditions for pressure and normal velocity. This type of boundary invariably generates some sort of artificial wave reflection upon the arrival of waves from the interior of the computational grid. It has no resetting or self-correcting capability, so there is no reason to expect that it will return to some "correct" value after being perturbed, even if the computation is carried out for a long time relative to the hydrodynamic events being simulated.

##### B. Transmissive Boundary Check.

The computations labelled SS/TB1 through SS/TB5 were used to quantify the effects of moving only the top transmissive boundary in the 2-D Cartesian grid. ("TB" refers to Top Boundary and "n" to the computation number.) The location of the upstream constant-inflow boundary was kept constant at 24.37 m from the front face of the target. The location of the downstream simple transmissive boundary was kept constant at 22.98 m from the back face of the target. SS/TB1 was run for 610 ms simulated real time, with the top transmissive boundary of the grid located 12.51 m from the top flat section of the target. SS/TB2 was run for 300.2 ms (top boundary at 27.03 m), SS/TB3 for

300.0 ms (top boundary at 41.55 m), SS/TB4 for 610.1 ms (top boundary at 56.08 m), and SS/TB5 was run for 610.2 ms (top boundary at 85.12 m). SS/EB5 was run for 610.1 ms, with a top boundary location equal to that of SS/TB5, but with the upstream inflow boundary located 135.30 m from the front face and the downstream boundary located 128.63 m from the back face. These data and other descriptive data are summarized in Table 1.

The computational flow field cells which comprise target SS and its immediate vicinity range from 26.40 to 22.47 cm in the direction of shock travel and are 15.24 cm in height. Overall, the target was resolved by 12 cells in depth and 12 cells in height. Each succeeding computation in the TBn series described above contained the previous computational flow field as a subset. SS/TB1 had a total of 86 flow field cells in the direction of shock travel and 48 cells in height, SS/TB2 contained 86 by 68, SS/TB3 86 by 88, SS/TB4 86 by 108, SS/TB5 86 by 148, and SS/EB5 246 by 148. SS/EB5 contained SS/TB5 as a subset.

One of the first considerations in the design of a grid is to determine the probable amount of disturbance-free time in the region of interest that can be simulated. After the planar incident shock strikes the front face of the target, a strong, planar, reflected shock is sent upstream at a velocity,  $v_r$ , relative to the oncoming flow. The gas immediately behind the reflected shock just after its creation is at rest. An expansion or weak compression wave in this region travels at the local speed of sound,  $c_r$ . If the extreme case is considered where there is no attenuation of this reflected shock, hereinafter called Upstream Assumption 1 (UAL), then the travel time,  $t_{uf1}$ , required to go from the front face to the upstream boundary is,

$$t_{uf1} = \frac{d_f}{v_r - v_s} . \quad (1)$$

Here,  $d_f$  is the distance from the front face to the upstream boundary and  $v_s$  is the particle velocity of the gas that has been processed by the incident shock. The travel time,  $t_{df1}$ , required to go downstream from the upstream boundary to the front face is

$$t_{df1} = \frac{d_f}{c_r} . \quad (2)$$

Assumption UAL predicts an upstream travel time of 73 ms and a downstream travel time of 49 ms for a total disturbance-free time of 122 ms for the TBn series. The comparable times for SS/EB5 are 405 ms upstream and 272 ms downstream for a total travel time of 677 ms.

The more reasonable assumption is that the reflected shock will decay in strength as it expands upstream from the target. Upstream Assumption 2 (UA2) adopts the extreme position that the effect of the reflected shock on wave propagation between the upstream boundary and the front face is negligible. Therefore, the travel time,  $t_{uf2}$ , (front face to upstream boundary) is

$$t_{uf2} = \frac{d_f}{c_s - v_s} , \quad (3)$$

Table 1. Hydrocode Computations

Identification	Computation Number	Time Simulated (ms)	Flow Field Cells			Active Space Around Target (m)		
			I	J	K	Front to Boundary	Back to Boundary	Top to Boundary
SS/TB1	8403.16	610.0	86	48	-	24.3686	22.9819	12.5065
SS/TB2	8407.11	300.2	86	68	-	24.3686	22.9819	27.0300
SS/TB3	8407.12	300.0	86	88	-	24.3686	22.9819	41.5535
SS/TB4	8407.13	610.1	86	108	-	24.3686	22.9819	56.0769
SS/TB5	8408.16	610.2	86	148	-	24.3686	22.9819	85.1239
SS/EB5	8408.17	610.1	246	148	-	135.3012	128.6321	85.1239
SS/3-D	8403.21	130.0	49	5	86	24.3686	22.9819	13.2327
RT/L-R	8402.10	300.1	86	48	-	24.3686	22.9819	12.5065
RT/H-R	8402.07	130.0	224	170	-	21.7222	21.1945	18.3304

where  $c_s$  is the local speed of sound behind the incident shock. The travel time,  $t_{df2}$ , (upstream boundary to front face) is

$$t_{df2} = \frac{d_f}{c_s + v_s} . \quad (4)$$

Assumption UA2 predicts an upstream travel time of 296 ms and a downstream travel time of 32 ms for a total travel time of 328 ms for the TBn series. The comparable times for SS/EB5 are 1.644 s upstream and 0.177 s downstream for a total travel time of 1.821 s.

Assumptions UA1 and UA2 represent the two extremes of the possible arrival time at the front face of a disturbance travelling this out-and-return path. It seems logical that the actual disturbance-free time must lie between these two extremes. The two assumptions may be combined into a more general assumption, UA3, that the reflected shock makes some fractional modification to the average wave propagation velocities in the region upstream from the front face. It is proposed that the travel time,  $t_{uf3}$ , (front face to upstream boundary) is

$$t_{uf3} = \frac{d_f}{xv_r + (1-x)c_s - v_s} , \quad (5)$$

and the travel time,  $t_{df3}$ , (upstream boundary to front face) is

$$t_{df3} = \frac{d_f}{xc_r + (1-x)(c_s + v_s)} . \quad (6)$$

The factor,  $x$ , in Equations (5) and (6) represents the fractional contribution of the reflected shock to the upstream wave velocities and is limited to a range of values from zero to one. The limiting case where  $x = 1$  is consistent with UA1 and  $x = 0$  is consistent with UA2. The value of  $x$  will depend upon the geometry of both the target and the computational grid.

The reflected shock in this 2-D problem very quickly takes on the shape of a right-circular cylinder. The surface of a cylinder varies linearly with radius, and the travel from the target face to the upstream boundary represents one half of the total distance travelled. The initial "radius,"  $r$ , of the reflected shock is taken as the radius of a semi-circle having the same area as the cross-sectional area of the target. The final radius of the reflected shock is taken as  $(d_f + r)$ . The initial radius divided by the final radius is taken as the contribution of the reflected shock,  $x$ , where

$$x = \frac{r}{d_f + r} . \quad (7)$$

Equation (5) yields an upstream travel time of 254 ms and Equation (6) yields a downstream travel time of 34 ms for a total predicted time of 278 ms for disturbances to travel from the front face to the upstream boundary and return. This applies to all computations in the TBn series. The comparable times for SS/EB5 are 1.581 s upstream and 178 ms downstream for a total travel time of 1.759 s.

The disturbance-free time for the back face (relative to artificial wave arrivals from the downstream boundary) may be computed more easily than that for the front face. The travel time,  $t_{db}$ , of the incident shock from the plane of the front face ( $t = 0$  there) to the back boundary is

$$t_{db} = \frac{d_b + d_{tgt}}{v_s}, \quad (8)$$

where  $d_b$  is the distance from the back face to the downstream boundary,  $v_s$  is the incident shock velocity, and  $d_{tgt}$  is the target depth. The travel time,  $t_{ub}$ , (back boundary to back face) is

$$t_{ub} = \frac{d_b}{c_s - v_s}. \quad (9)$$

Equation (8) yields a downstream travel time of 43 ms and Equation (9) yields an upstream travel time of 279 ms for a total disturbance-free time of 322 ms for the back face relative to the downstream boundary. These times apply to all computations in the TBn series. The comparable times for SS/EB5 are 217 ms downstream and 1.563 s upstream for a total disturbance-free time of 1.780 s.

An analysis similar to that for the front face can be made for predicting the arrival time at the top face of the target of a disturbance from the top boundary. A lower limit can be established for the travel time of disturbances between the top face of the target (taken for simplicity to be the center of the top flat section) and the top boundary. Top Assumption 1 (TA1) is that the time,  $t_{tl}$ , (top face to top boundary and return) is

$$t_{tl} = \frac{2d_t}{c_s}, \quad (10)$$

where  $d_t$  is the distance from the top face to the top boundary. Equation (10) predicts a lower-limit disturbance-free time of 59 ms for SS/TB1, 128 ms for SS/TB2, 196 ms for SS/TB3, 265 ms for SS/TB4, and 402 ms for SS/TB5 and SS/EB5.

Making the assumption that there is no contribution from the reflected shock, waves moving between the top boundary and top face will have a velocity component equal to  $v_s$  imposed on them, thereby increasing their required travel time and distance. Top Assumption 2 (TA2) is that the disturbances likely to arrive first at the top face (when considered alone) are those which have originated at the top face and have travelled upstream at an angle (relative to the normal vector of the top flat section) whose tangent may be computed by

$$(\tan\theta)_2 = \frac{v_s}{c_s}. \quad (11)$$

The time,  $t_{ut2}$ , required for a disturbance to travel to this limiting upstream point on the top boundary is

$$t_{ut2} = \frac{d_t}{c_s} + \frac{(d_t)\tan\theta}{c_s - v_s}. \quad (12)$$

The time,  $t_{dt2}$ , required for a disturbance to return from this point is

$$t_{dt2} = \frac{d_t}{c_s} + \frac{d_t \tan \theta}{c_s + v_s} . \quad (13)$$

Equations (11), (12), and (13) yield combined travel times of 195 ms for SS/TB1, 421 ms for SS/TB2, 647 ms for SS/TB3, 873 ms for SS/TB4, and 1.326 s for SS/TB5 and SS/EB5.

A more probable assumption would be similar to that used for the upstream timing analysis. Top Assumption 3 (TA3) is that there is a fractional contribution,  $y$ , from the reflected shock, where

$$y = \frac{r}{d_t + r} . \quad (14)$$

Equations (11), (12), and (13) are modified as follows, with all terms retaining their previous definitions and  $y$  limited to a range of values from zero to one.

$$(\tan \theta)_3 = \frac{v_s(1-y)}{c_s(1-y)+yc_r} \quad (15)$$

$$t_{ut3} = \frac{d_t}{c_s(1-y)+yc_r} + \frac{d_t \tan \theta}{(c_s-v_s)(1-y)+yc_r} \quad (16)$$

$$t_{dt3} = \frac{d_t}{c_s(1-y)+yc_r} + \frac{d_t \tan \theta}{(c_s+v_s)(1-y)+yc_r} . \quad (17)$$

A value of  $y = 0$  is consistent with TA2, and a value of  $y = 1$  is the degenerate case where a shock strikes the closed end of a constant-area tube. For SS/TB1,  $y = 0.124$  and the angle from Equation (15) is 34.63 degrees measured counterclockwise from the vertical. Equations (15), (16), and (17) yield combined travel times of 134 ms for SS/TB1, 341 ms for SS/TB2, 558 ms for SS/TB3, 779 ms for SS/TB4, and 1.226 s for SS/TB5 and SS/EB5. The arrival times predicted by the various methods of the artificial waves from the transmissive boundaries are shown in Table 2.

Figure 2 shows the average overpressure on the front face of target SS for SS/TB1 through SS/TB5. Also shown in Figure 2 is a curve for SS/EB5. SS/EB5 will be used as a reference computation to assist in identifying the arrivals of waves from the top boundary in the TBn series of computations, and will itself later be used to illustrate a significant defect in HULL's ability, at least for a non-decaying shock and with this flow-field resolution, to properly model the strong vortex to be expected behind a blunt 2-D target such as this one. (The late time loading in SS/EB5 is too high for all faces except the front face and possibly the front slope because of the improper modelling of this vortex, which causes an excessively strong flow to impinge on the back face of SS.)

Table 2. Predicted Arrival Times of Artificial Waves from Boundaries

Computation	Front			Top			Back		
	Prediction Method $\frac{UA1}{(s)}$	Prediction Method $\frac{UA2}{(s)}$	Prediction Method $\frac{UA3*}{(s)}$	Prediction Method $\frac{TA1}{(s)}$	Prediction Method $\frac{TA2}{(s)}$	Prediction Method $\frac{TA3*}{(s)}$	Prediction Method $\frac{TA1}{(s)}$	Prediction Method $\frac{TA2}{(s)}$	Prediction Method $\frac{TA3*}{(s)}$
SS/TB1	0.122	0.328	0.278	0.059	0.195	0.134			0.322
SS/TB2	0.122	0.328	0.278	0.128	0.421	0.341			0.322
SS/TB3	0.122	0.328	0.278	0.196	0.647	0.558			0.322
SS/TB4	0.122	0.328	0.278	0.265	0.873	0.779			0.322
SS/TB5	0.122	0.328	0.278	0.402	1.326	1.226			0.322
SS/EB5	0.677	1.821	1.759	0.402	1.326	1.226			1.780

\*Probable time.

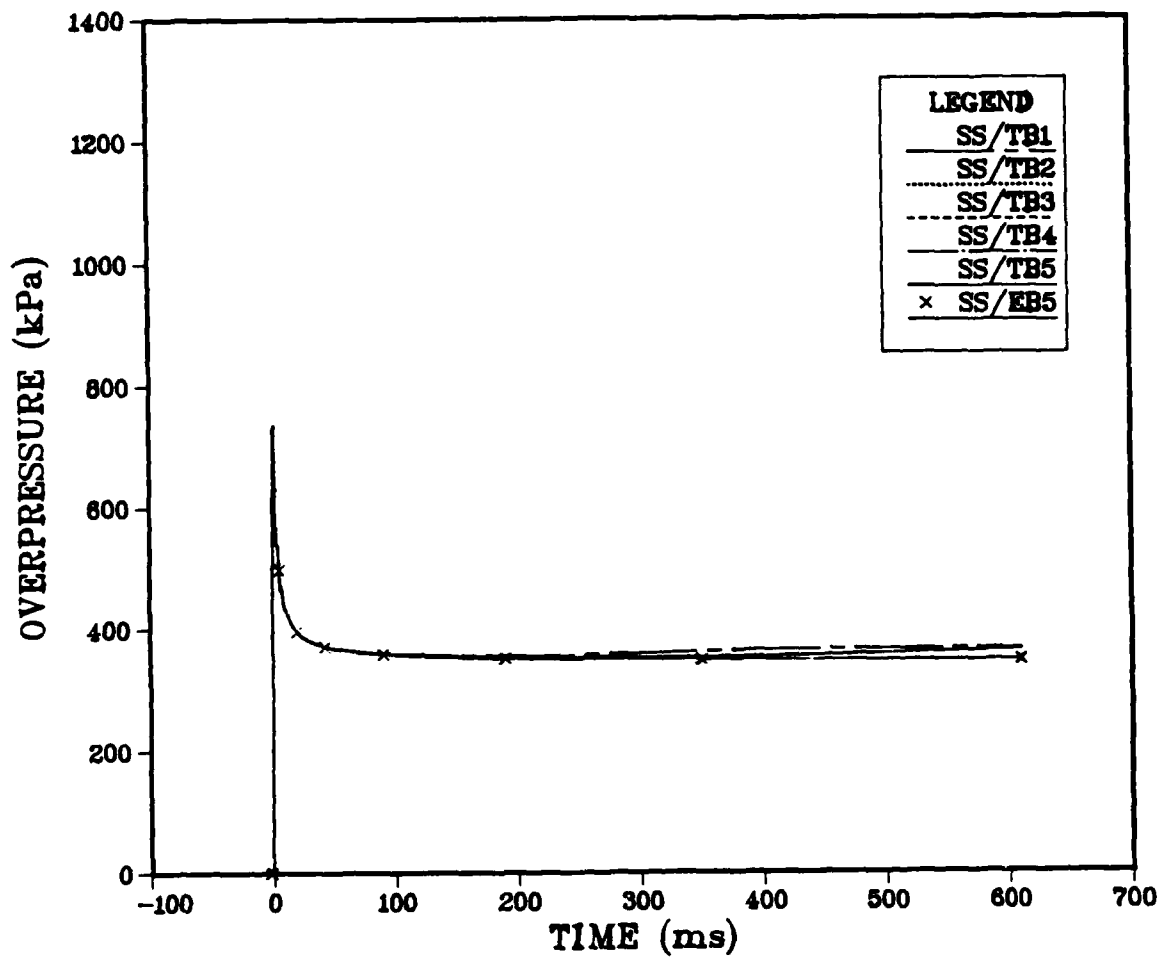


Figure 2. Boundary Check Computations for Average Overpressure on the Front Face.

Computation SS/TB1 shows a divergence from both SS/TB5 and SS/EB5 caused by a compression wave arrival from the top boundary at 110 ms. (A wave arrival is considered as confirmed once the average overpressure values from a computation have deviated by 0.5 percent or more from those for a reference computation.) Until that time, all computations are in agreement. Computations SS/TB2, SS/TB3, and SS/TB4 all show agreement with SS/TB5 throughout their respective run times. The next deviations from computation SS/EB5 are by SS/TB2 at 270 ms and by SS/TB3, SS/TB4, and SS/TB5 at 290 ms, due primarily to compression wave arrivals from the upstream boundary. Except for an obvious interference from the top boundary for SS/TB1, the artificial wave arrivals correlate well with the predicted time of 278 ms from UA3 for the TBn series. It appears that SS/EB5 provides a reliable estimate for both the diffraction phase and drag phase average overpressure on the front face. Table 3 provides a summary of the first deviations of SS/TB1 through SS/TB4 from SS/TB5 for this face and all other faces. These deviations are direct indicators of the effects of the locations of the top boundary. Table 4 provides a similar summary of the first deviations of the TBn series from SS/EB5 for all faces, thus showing the superimposed effects of the locations of the upstream and downstream boundaries.

Table 3. First Deviation from SS/TB5

<u>Computation</u>	Front Face (ms)	Front Slope (ms)	Top Flat Section (ms)	Back Slope (ms)	Back Face (ms)
SS/TB1	110	100	80	75	75
SS/TB2	*	270	180	180	170
SS/TB3	*	*	270	290	290
SS/TB4	*	490	390	390	390

\*Agreement through its end of run time.

Table 4. First Deviation from SS/EB5 (Reference)

<u>Computation</u>	Front Face (ms)	Front Slope (ms)	Top Flat Section (ms)	Back Slope (ms)	Back Face (ms)
SS/TB1	110	100	80	75	75
SS/TB2	270	290	130	130	120
SS/TB3	290	250	130	130	120
SS/TB4	290	250	130	130	120
SS/TB5	290	250	130	130	120

Figure 3 shows the average overpressure on the front slope. There is more variation evident in these curves because of the orientation of the front slope relative to the top boundary. SS/TB1 shows an initial slight deviation from SS/TB5 at 100 ms, a return to relative agreement, then a permanent deviation starting at 200 ms. The deviations at 100 and 200 ms appear to be due to the arrival of compression waves from the top boundary. There is also an arrival of an artificial expansion wave at 440 ms. SS/TB2 deviates from SS/TB5 at 270 ms, not long before its ending of 300.2 ms, and SS/TB3 matches SS/TB5 throughout its 300 ms run time. SS/TB4 does not diverge from SS/TB5 until 490 ms. This can only be due to a difference in top boundary effects as far as these two computations are concerned. However, there is more here that

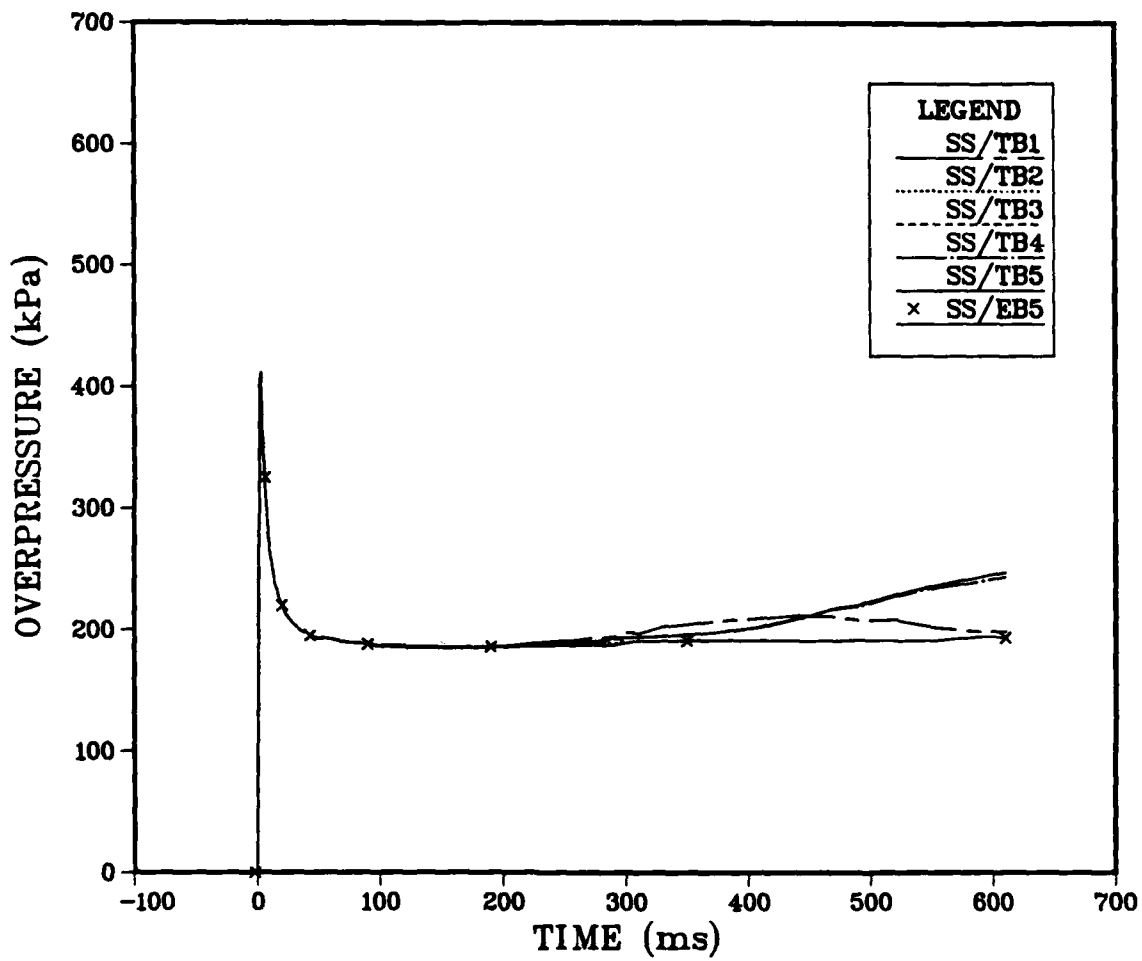


Figure 3. Boundary Check Computations for Average Overpressure on the Front Slope.

is of interest. The only differences between SS/TB5 and SS/EB5 are the locations of the upstream and downstream boundaries. The joint divergence of SS/TB4 and SS/TB5 from SS/EB5 for the front slope occurs at 250 ms, so this divergence must therefore be due to an artificial compression wave from the upstream boundary. SS/EB5 also shows a distinct wave arrival at 290 ms, with a small cusp-like feature at 310 ms. From the earlier discussion on the timing of disturbance arrivals, it is very unlikely to have originated from any of the transmissive boundaries. It is possible that it is from a recompression following an over-relief of the initial shock reflection, but that is speculative, and the timing seems late for that. At present, the best that can be said is that it probably originates from an unknown upstream source.

Figure 4 shows the set of curves for average overpressure on the top flat section. SS/TB1 shows the arrival of an expansion wave from the top boundary at 80 ms, followed by some combination of compression waves arriving at about 160 ms from the top boundary upstream from the target. These compression waves plus others from the upstream and downstream boundaries form an artificial peak of 159 kPa in the overpressure curve by 410 ms, 27 percent above the 125 kPa overpressure at the same time for SS/EB5. SS/TB2 shows the arrival of a weak expansion wave from the top boundary at 180 ms, fortuitously cancelled by an artificial compression wave so that it remained close to the curve for SS/EB5. SS/TB3 shows only the beginning of an artificial expansion wave at 270 ms, and SS/TB4 shows a weak expansion wave arrival at 390 ms. Thus, there is a definite correlation between the expansion wave arrival in the TBn series and the top transmissive boundary location. A comparison between SS/TB5 and SS/EB5 shows that a weak compression wave influences the results for SS/TB5 between 130 ms and 320 ms. This is also true for both SS/TB3 and SS/TB4. The strong compression wave at 320 ms is clearly due to a reflection from the downstream boundary. However, the compression wave arrival at 130 ms was initially quite puzzling because the preceding analysis showed no realistic probability of wave arrivals from the transmissive boundaries at such an early time. The key to understanding this compression wave arrival is in the artificial, unbounded downstream growth of the vortex at the back face. (This will be discussed in detail later in the section on SS/EB5. Only the specifics necessary to understand this wave arrival will be discussed here.) The artificially large back face vortex lengthens in the downstream direction at 120 m/s (the rate of progression of its downstream end with time), while its upstream end remains at the back face. It generates an excessively strong reverse flow along the ground plane, having a velocity of 200 m/s directed at the back face. A relatively straightforward timing check indicates that the incident shock arrives at the downstream boundary at 43 ms, sends an artificial compression wave upstream which meets the end of the vortex at 109 ms at a point 12 m downstream from the back face, and rides upstream on the reverse flow of the vortex, arriving at the back face at 128 ms. This is essentially an exact match in time with the observed disturbance at 130 ms on the top flat section. This disturbance was not seen in SS/TB1 because waves from the top boundary washed out that effect; it is missing from SS/EB5 because of the remote downstream boundary. There is also a slight cusp-like feature in SS/EB5 at 310 ms, essentially at the same time as the cusp for the front slope average overpressure for SS/EB5 shown in Figure 3, but noticeably weaker. This lends support to the conclusion that the wave which produced it originates from an upstream source.

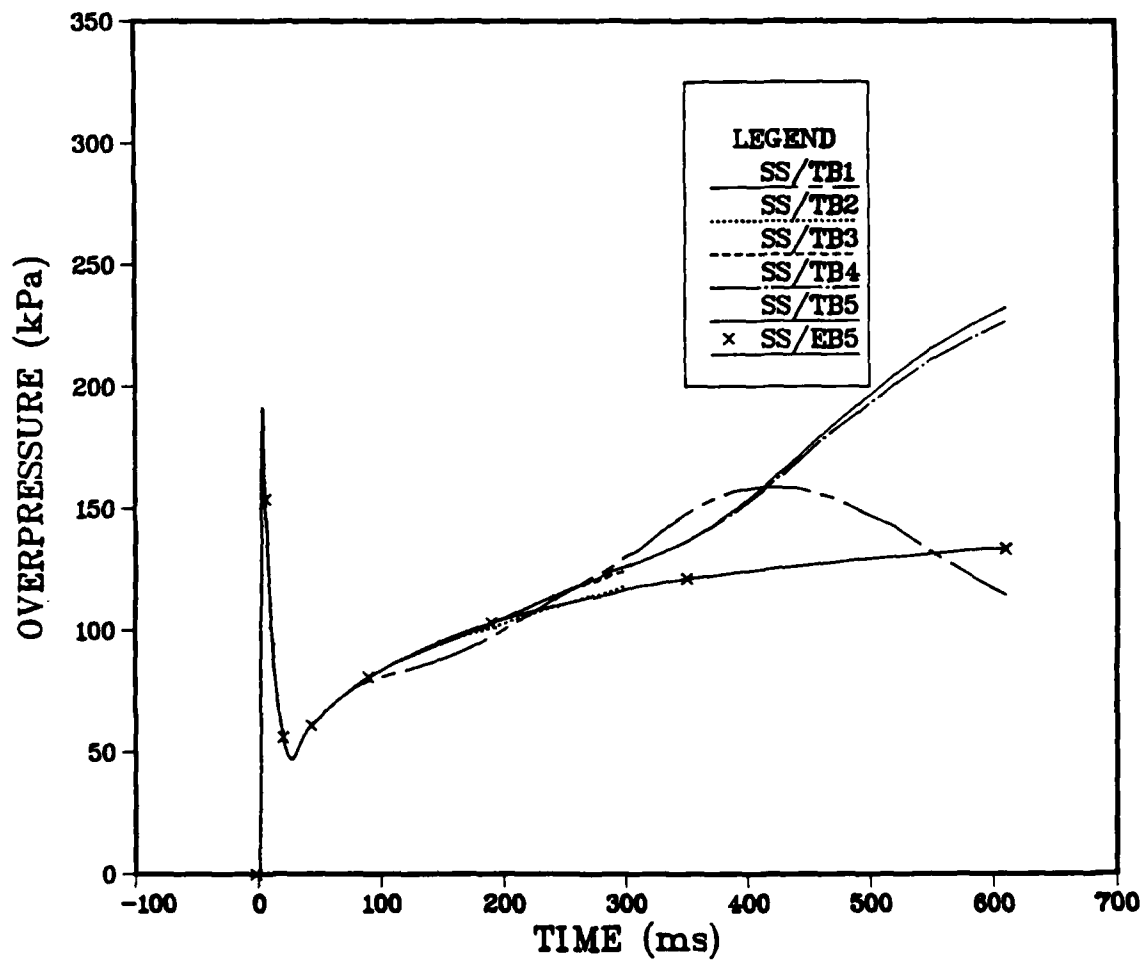


Figure 4. Boundary Check Computations for Average Overpressure on the Top Flat Section.

Figure 5 shows the average overpressure versus time on the back slope of target SS. All computations show an initial pressure peak of 112.9 kPa at 6 ms, 45.4 percent below the incident shock overpressure of 206.8 kPa because of the 30 degree negative angle of the back slope relative to the undisturbed flow. This peak is followed by a sharp drop to a minimum value of 27.2 kPa at 15 ms because of the vortex that forms off the trailing edge of the flat section on the top face. All computations are in agreement through 80 ms, when SS/TB1 shows the arrival of the artificial expansion wave from the top boundary. The subsequent performance of SS/TB1 is similar to that on the top flat section, as are the rest of the curves in the TBn series. The other initial artificial expansion wave arrivals are at 180 ms for SS/TB2, 290 ms for SS/TB3, and 390 ms for SS/TB4. The comments concerning the compression wave arrivals at 130 ms and 320 ms that were made for the top flat section also apply here. It is also interesting that SS/EB5 for the back slope does not show the cusp-like feature at 310 ms, shown clearly for the front slope and weakly for the top flat section. This confirms its upstream origin. The artificial wave arrivals relative to SS/TB5 shown for the front slope, top flat section, and back slope indicate that TA1 gives too low an estimate of wave arrival time and TA3 too high an estimate, with TA1 somewhat closer to the actual values on average.

Figure 6 shows the average overpressure on the back face of the target. All computations agree through the first 75 ms, showing a relatively sharp rise to a local maximum of 101.1 kPa at 20 ms, and then a brief drop to a local minimum of 98.8 kPa at 30 ms. SS/TB1 shows the arrival of an expansion wave at 75 ms, completing an interesting progression of initial wave arrivals on the various faces of target SS: expansion waves at 75 ms for the back face, 75 ms for the back slope, and 80 ms for the top flat section; and compression waves at 100 ms for the front slope and 110 ms for the front face. Thus, the initial disturbances due to compression waves on the front face and front slope originate from a region of the top boundary upstream from the target. The initial disturbances due to expansion waves on the top flat section, the back slope, and the back face originate from a region of the top boundary closer to the target.

The initial expansion wave which arrives at the back face of target SS in SS/TB1 at 75 ms is followed by a recompression starting at 150 ms. This recompression peaks at 201 kPa overpressure by 410 ms before it drops due to another expansion wave, most likely originating from the top boundary. (This strong expansion wave is absent in SS/TB4 and SS/TB5.) The recompression before 350 ms is due to compression waves from the top boundary and the downstream vortex action discussed earlier, and after 350 ms is due to a compression wave from the incident shock interaction with the downstream boundary. SS/TB2 for the back face of target SS in Figure 6 shows a weak expansion wave arrival at 170 ms, 10 ms ahead of the arrival of the initial expansion wave for the back slope, which is consistent with the pattern noted for SS/TB1. SS/TB3 shows a weak initial expansion wave at 290 ms, and SS/TB4 shows an expansion wave arrival relative to SS/TB5 at 390 ms. Both computations show the arrival of a very weak expansion wave at 120 ms relative to SS/EB5. The flow on the back face has become exaggerated by this time, as will be shown later, so this may not be outside of the realm of possibility. The flow is recompressed by the wave moving up the vortex starting at 160 ms and by a strong compression wave from the downstream boundary at 350 ms. In

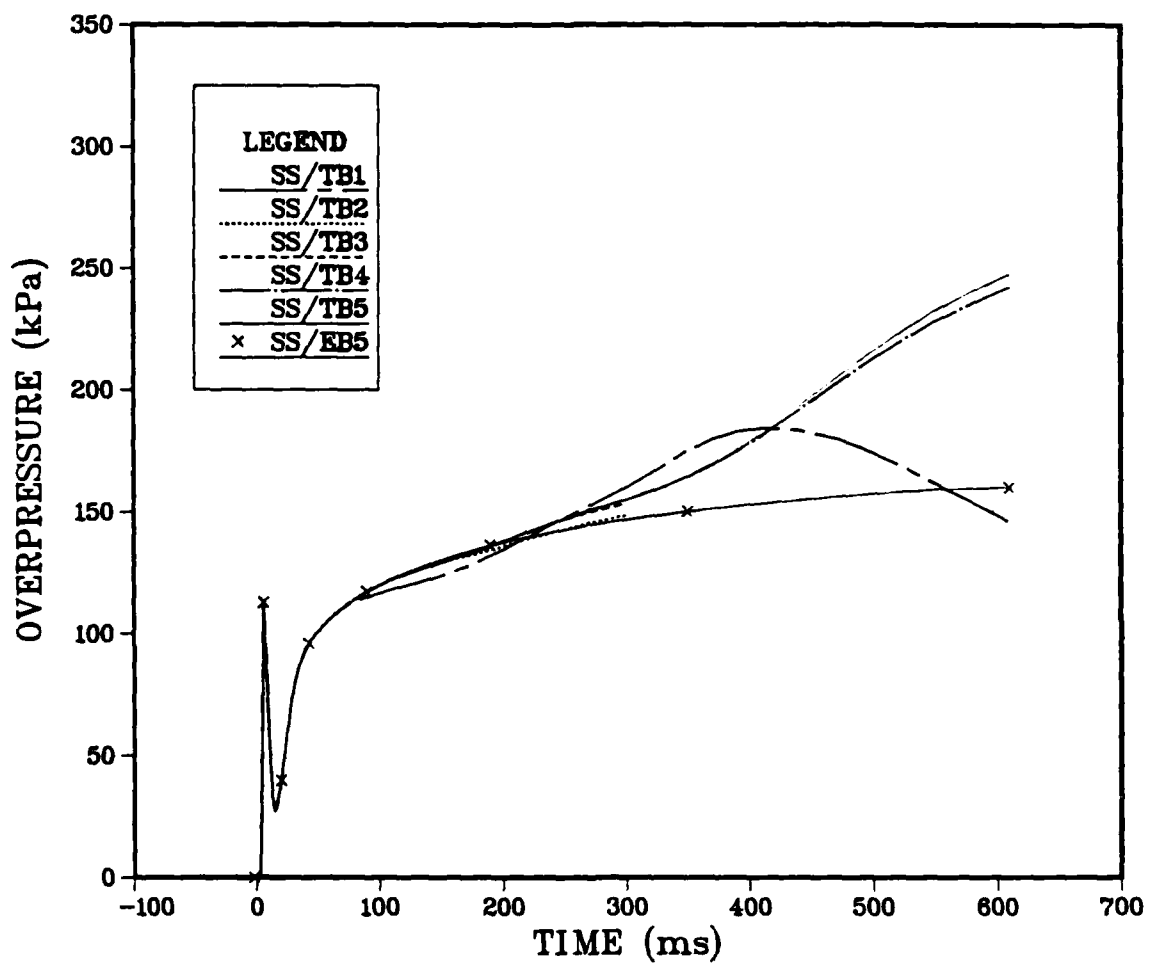


Figure 5. Boundary Check Computations for Average Overpressure on the Back Slope.

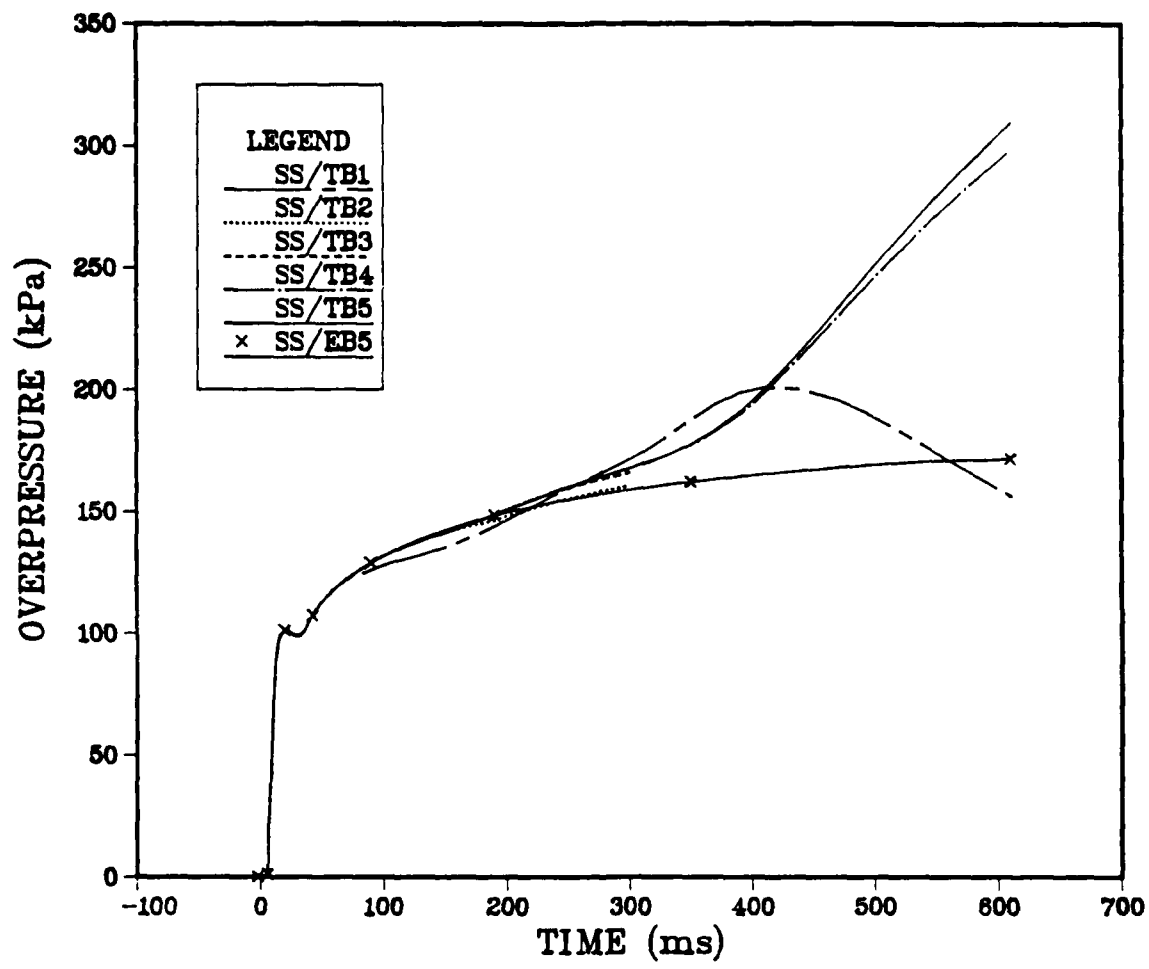


Figure 6. Boundary Check Computations for Average Overpressure on the Back Face.

the absence of top boundary effects, the predicted 322 ms arrival time of artificial waves from the downstream boundary for the TBn series appears to be of acceptable accuracy.

#### C. Extended Boundary Reference Computation SS/EB5.

As indicated earlier, although SS/EB5 is useful as a reference computation for the TBn series in the previous subsection, its modelling of the vortex behind target SS at late time is not correct. Figure 6, for example, shows that the average overpressure on the back face from SS/EB5 is steadily increasing with time. The ending time of 610.1 ms for SS/EB5 represents 121.5 shock crossing times. (A shock crossing time is defined as the time required for the incident shock to travel from the plane of the front face to the plane of the back face.) This number of shock crossing times should be more than sufficient for a steady state loading to be reached, yet SS/EB5 still shows a significant positive slope in the average overpressure versus time curve at its ending time.

Figure 7a shows a close-up view of the velocity vectors at 10 ms in the flow field in the vicinity of target SS. This is relatively soon after the shock has passed over the target, and the downstream recirculation region has not yet developed. Figure 7b shows the same region at 20 ms. The recirculation region has just begun to form, with its center of rotation located 0.7 m downstream from the back face. Its scale and location appear to be quite reasonable. Figure 7c shows the downstream recirculation region fully formed by 30 ms, with its center 1.7 m, or 0.56 target depths, downstream from the front face. The reverse flow near the ground plane is beginning to impinge strongly on the back face, raising the pressure there and also on the back slope. The pressure rise on the back slope is high enough that the flow is turned away from it and is nearly parallel to the ground plane. By 40 ms, Figure 7d, the center of the recirculation region has moved to 2.6 m downstream from the back face. The recirculation region has an overall length of 4.5 m. The upstream counterflow is now impinging on the back face with sufficient strength that the pressure on the back face and back slope is high enough that the flow above the back slope has a significant positive vertical component. This seems to be the beginning of the artificially large downstream vortex. The vortex is centered at 2.8 m with an overall length of 5.0 m by 43 ms (Figure 7e), centered at 2.9 m with a length of 5.5 m by 46 ms (Figure 7f), and centered at 3.4 m with a length of about 6.0 m by 50 ms (Figure 7g). It is during this time from 40 to 50 ms that the computation in this region of the flow field loses credibility. The downstream vortex seems to grow without bound in the downstream direction, with a constant height of approximately 2.5 m. Figure 7h shows the local region of the flow field at the ending time of 610.1 ms. The "vortex" has evolved into a high-speed upstream flow along the ground plane, a low-speed layer above it, and then a top layer blending into the downstream flow above it, all extending tens of metres downstream from the target.

It seems unlikely that the center of the downstream recirculation region at the back face would extend more than the maximum dimension of the target, 3.05 m in depth for target SS. If this is accepted as a plausible criterion, then the latest time for "acceptable" results for the back face and back slope is 46 ms (see Figure 7f). Figure 8 shows the drag coefficient computed for target SS using the uncorrected loading for the front and back faces and

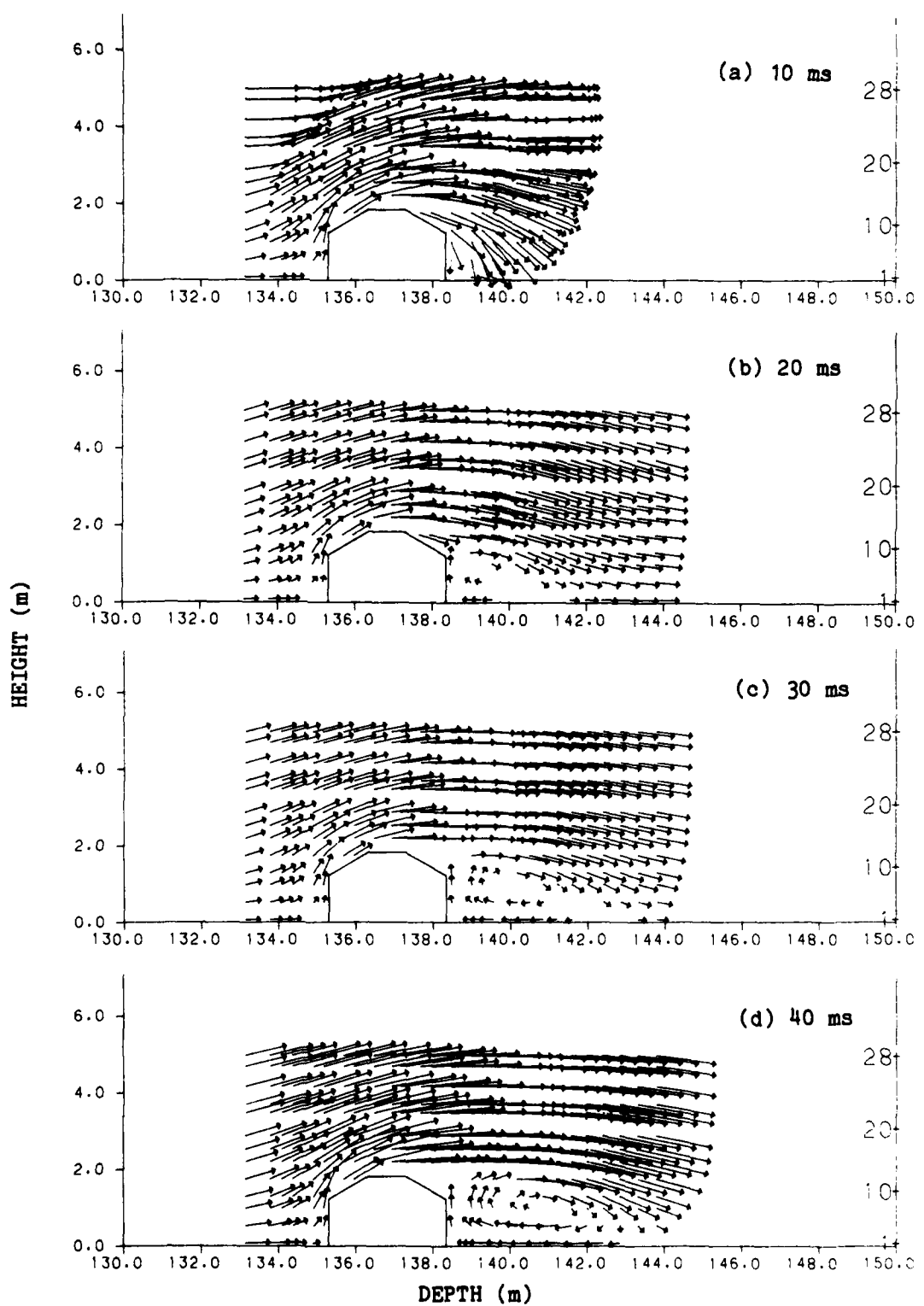


**Figure 7. Vortex Growth Behind the Back Face.**

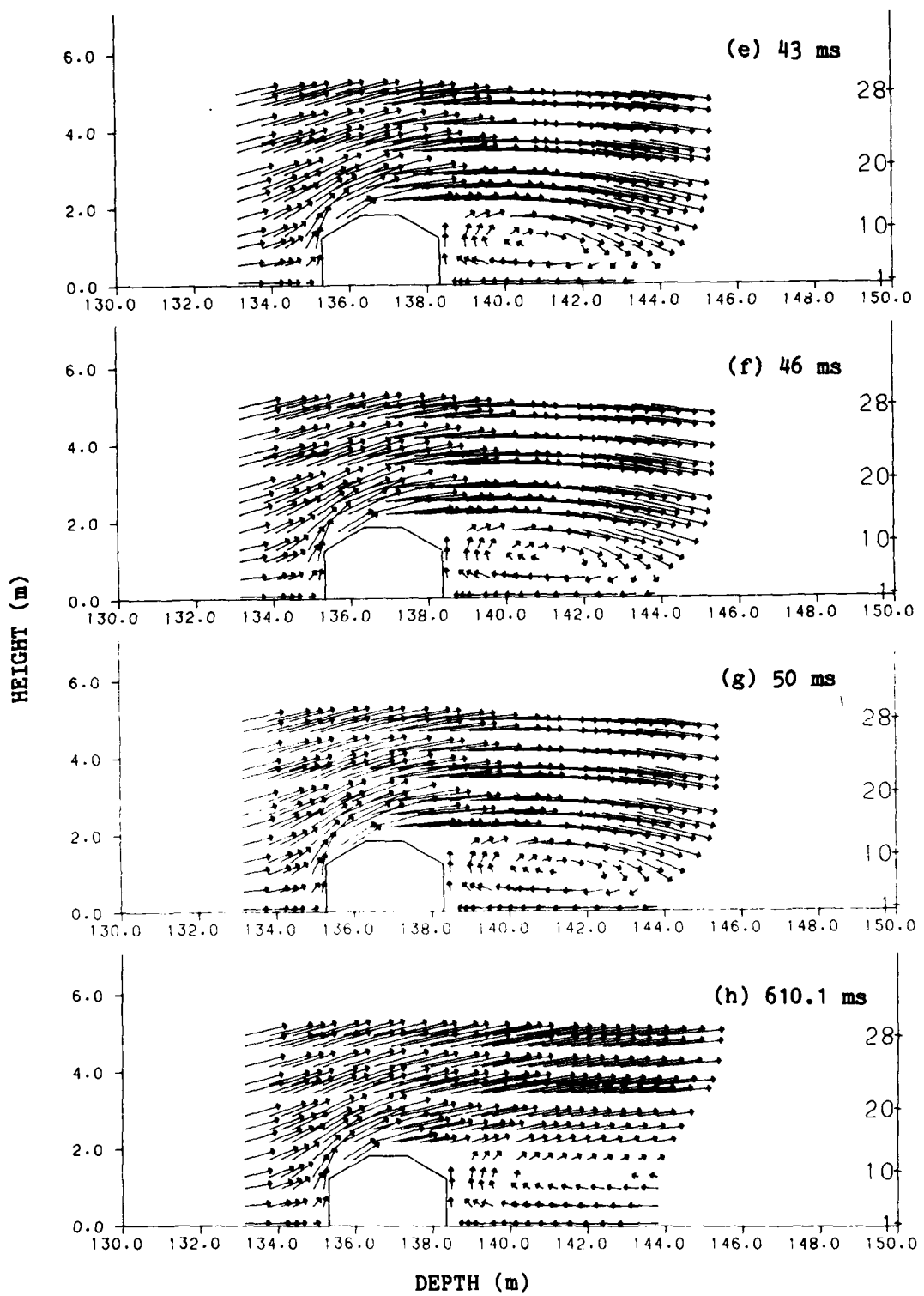


Figure 7. Vortex Growth Behind the Back Face (cont.).

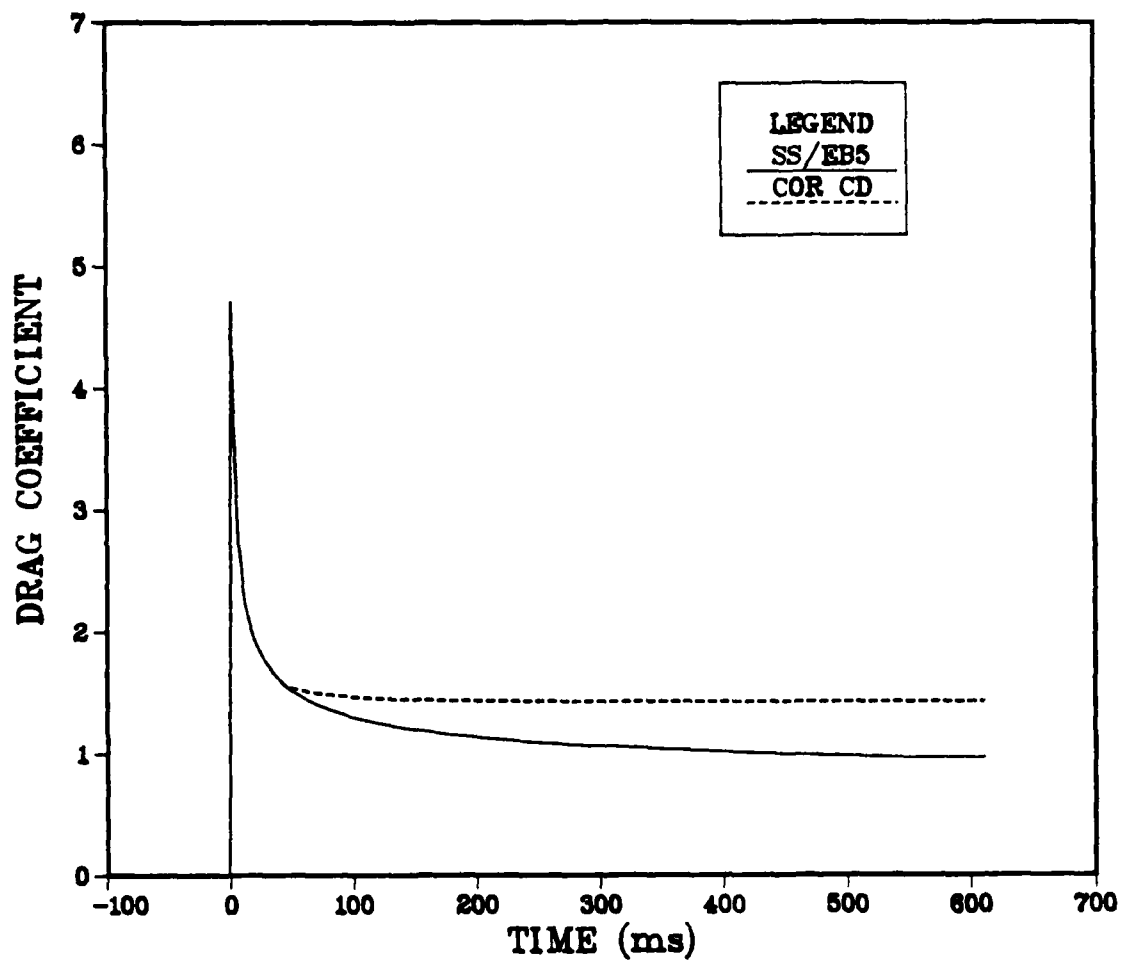


Figure 8. Corrected versus Uncorrected Drag Coefficient for SS/EB5.

slopes from SS/EB5, and the "corrected" drag coefficient. The corrected drag coefficient was computed by assuming that the front face and front slope loadings are acceptable up to 290 ms, and then constant at the 290 ms value for the remainder of the computation time to eliminate the effect of the artificial wave arrival discussed earlier. The loadings on the back face and back slope were assumed to be acceptable through 46 ms, then constant thereafter.

The drag coefficient as it is used here is actually an area-weighted pressure coefficient, taking the loading due to overpressure on the front as positive and that on the back as negative. This is also the sense in which the presentation of the drag coefficient for the diffraction phase as shown in Figure 8 should be taken. In this way, a curve that is complete in time is presented. This was also done a number of years ago by Tucker<sup>7</sup> in an evaluation of an earlier study<sup>8</sup> describing experimental drag coefficients for bluff bodies struck by non-decaying shocks.

The curve for drag coefficient in Figure 8 using the uncorrected overpressure falls steadily from its peak value of 4.70 during the diffraction phase, reaching the unacceptably low value of 0.96 at the 610.1 ms ending time. The curve using the corrected values matches the uncorrected curve through 46 ms; a steady, corrected drag coefficient of 1.42 is reached at 290 ms. This value seems to be plausible for this target, especially considering that HULL does not model viscosity at all. Some drag coefficients for simple shapes published by Hoerner<sup>9</sup> may be used as comparative guidelines. A plate mounted between parallel walls and oriented normal to a Mach 0.8 flow (the local Mach number behind the shock in the present study) has a drag coefficient of 2.2 (Reference 9, p.16-16), a 2-D square cross-section cylinder on a ground plane has a drag coefficient of 2.05 (ibid., p.3-17), and a right-circular cylinder in a Mach 0.8 cross-flow has a drag coefficient of 1.5 (ibid., p.16-16). The plate and square cylinder represent upper limits for the drag coefficient for target SS, and the circular cylinder represents a lower limit. If, for example, the drag coefficient computed from the corrected values for SS/EB5 is assumed to be too low by 10 to 20 percent (because of either undetected or uncorrected errors or simply the lack of viscous effects), then a quite consistent drag coefficient of from 1.56 to 1.70 is implied. Thus, it seems possible to estimate drag loading on targets with HULL, but only if great care is taken in interpreting the results. The far more preferable choice would be to use a hydrocode that is more complete in its approximation of the Navier-Stokes equations, particularly in regard to the inclusion of cross-derivative terms for better handling of rotational flows, and the inclusion of viscous effects.

#### D. Cross-Check of Computations.

The next set of figures shows comparisons between SS/TB1 and three similar computations: SS/3-D (Stair-Stepped target, 3-D coding), RT/L-R (Ramped Target, Low Resolution), and RT/H-R (Ramped Target, High Resolution). SS/3-D uses the same cross-section of target SS as used for the TBn series and is made hydrodynamically 2-D by using the 3-D coding with a five cell wide grid having perfectly-reflecting end planes; it has the same resolution as SS/TB1. Thus, a comparison between SS/TB1 and SS/3-D is a direct indicator of any systematic differences in results obtained by using the 2-D coding as opposed

to using the 3-D coding. RT/L-R uses target RT, which is identical to target SS except that the front and back slopes of RT are made smooth through the use of shore cells; it, too, has the same resolution as SS/TB1. A comparison between SS/TB1 and RT/L-R is a direct indicator of the effect of using stepped versus smooth slopes. The grid for RT/H-R was made by halving each flow-field cell in the grid for RT/L-R in each direction, a general doubling of resolution of RT/H-R over RT/L-R. Each of these computations has problems resulting from wave interactions with computational transmissive boundaries which may either have been exacerbated, unaffected, or mitigated by the variations introduced in target generation and resolution; those aspects of these computations will not be covered in this section.

Figure 9 shows the average overpressure on the front face for these four computations. There is little difference between the computations on this flat surface normal to the incident flow. Figure 10 shows the average overpressure on the front slope. SS/TB1 and SS/3-D show nearly identical results through the run time of SS/3-D. There is a large difference between RT/L-R and SS/TB1, which is directly attributable to modelling the slope as a smooth surface in RT/L-R. By 300 ms, the average overpressure on the front slope for SS/TB1 is 15 percent greater than for RT/L-R. The effects of shock interaction with stepped versus smooth surfaces has also been documented in other studies.<sup>2 10</sup> The doubled resolution of RT/H-R over RT/L-R produces a lower average overpressure on the front slope for RT/H-R. The average overpressure on the top flat section in Figure 11 shows a pattern similar to that on the front slope. RT/H-R apparently does the best at resolving the low-pressure vortex that forms off the leading edge of the flat section at early time. Figure 12 shows the average overpressure on the back slope. Here again SS/TB1 and SS/3-D show close agreement with each other. RT/L-R and RT/H-R agree very closely through the first 20 ms and then diverge, with RT/H-R showing a higher value by 130 ms. Figure 13 shows the average back face overpressure. SS/TB1 and SS/3-D show very close agreement, and share the lowest of the three initial peaks at 101 kPa. Interestingly, RT/L-R has the highest initial peak of 115 kPa, and RT/H-R has the intermediate peak of 110 kPa but has a value at 130 ms higher than that for RT/L-R. The overall effects of these variations are best seen in Figure 14, which shows the uncorrected drag coefficients for these four computations. There is essentially no difference between the drag coefficients for SS/TB1 and SS/3-D, RT/L-R tends to become slightly less than SS/TB1 and SS/3-D at later time, and RT/H-R is lower still.

This part of the study was intended to illustrate the potential for differences in computed loading at late time for this target and shock combination, depending on the method of target simulation and flow-field resolution. It would not be appropriate to use these four computations as a direct basis for applying a further correction to the drag coefficient computed from SS/EB5. The greater part of the divergence between these four computations shown in Figure 14 occurs after all four computations may be assumed to have some combination of errors due to either boundary effects or improper modelling of the downstream vortex.

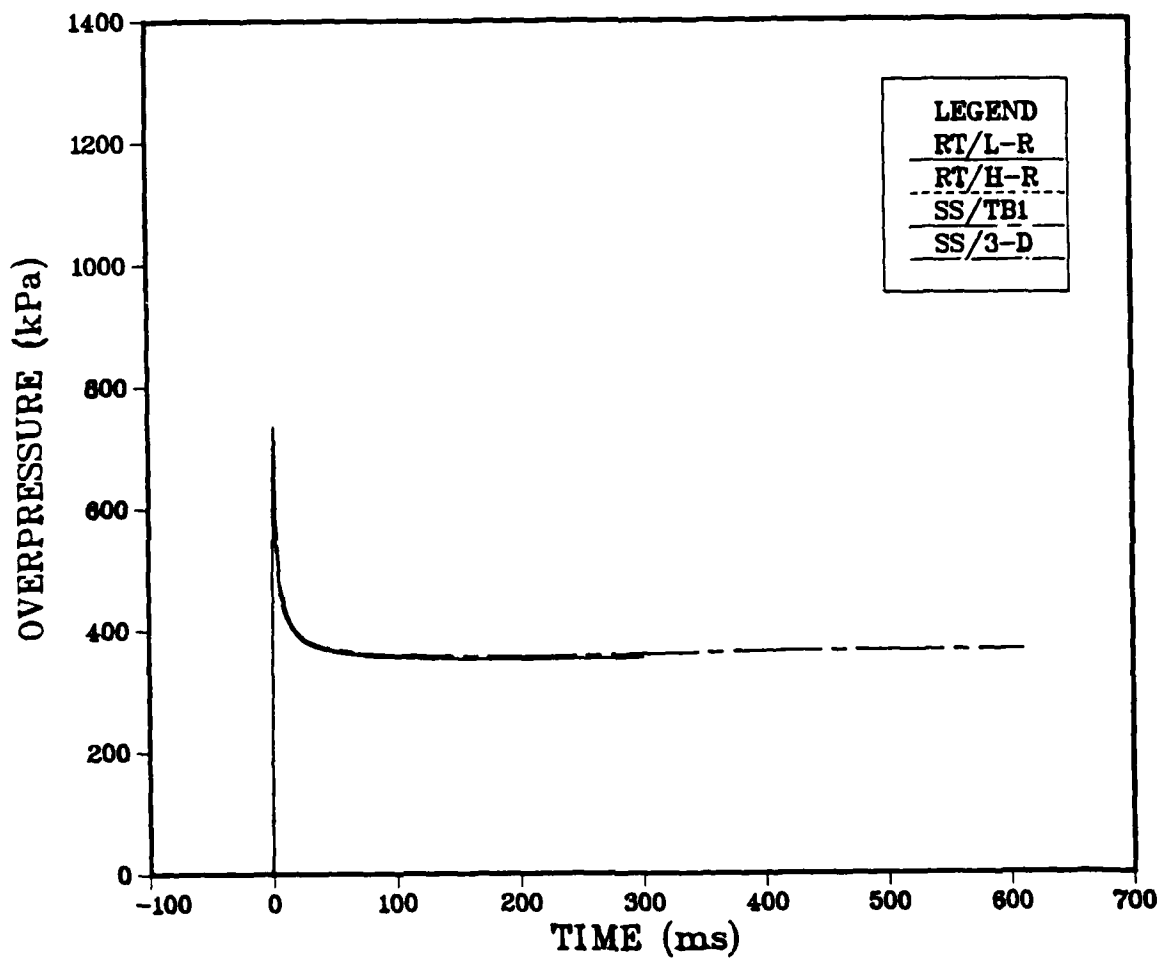


Figure 9. Comparison Computations for Average Overpressure on the Front Face.

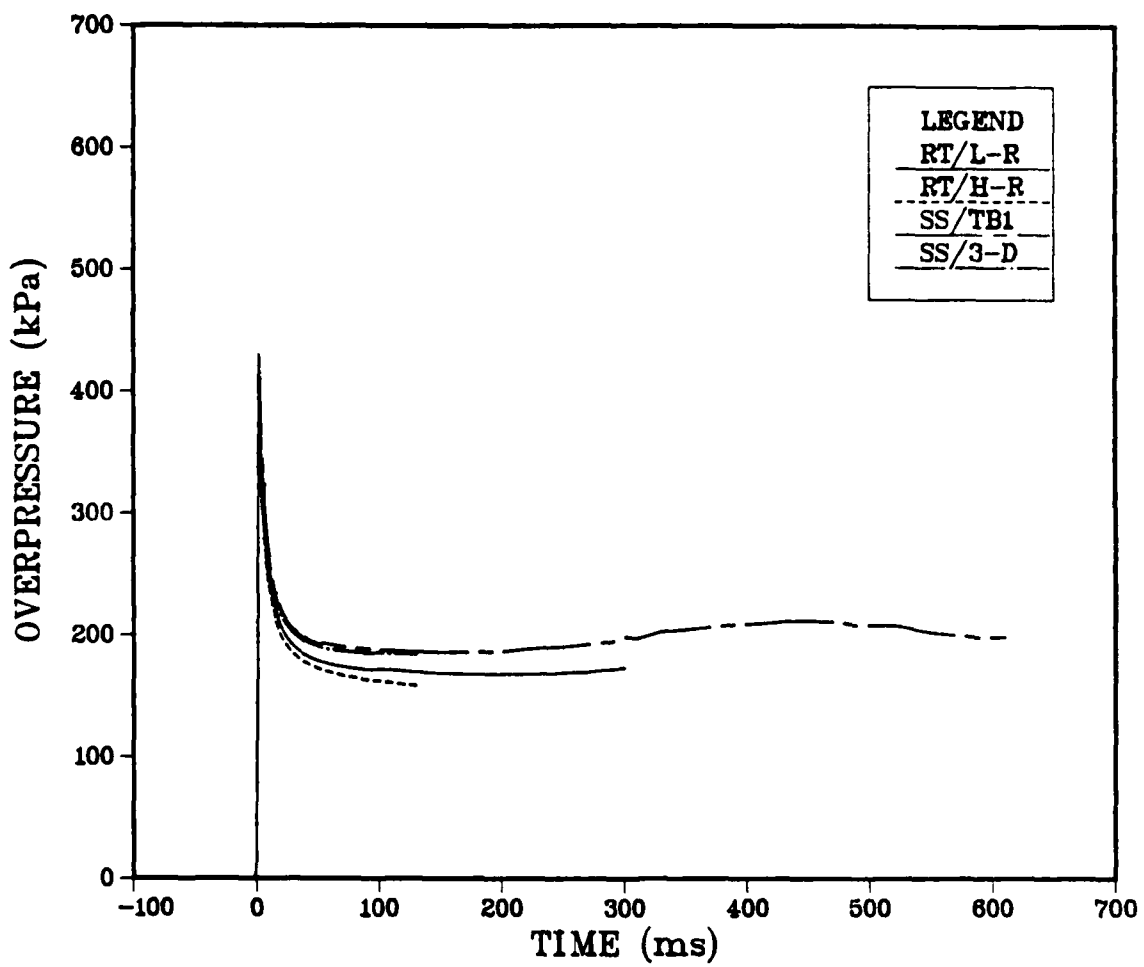


Figure 10. Comparison Computations for Average Overpressure on the Front Slope.

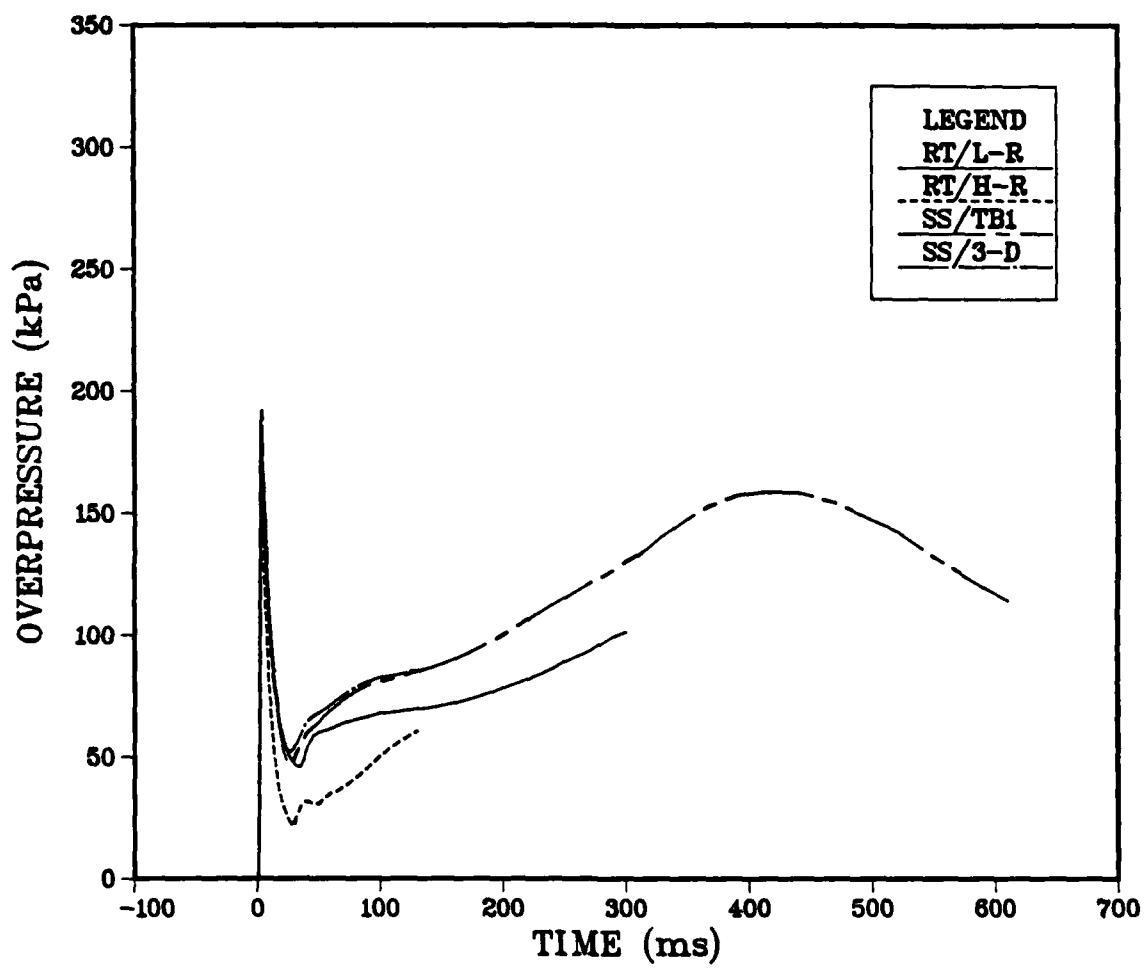


Figure 11. Comparison Computations for Average Overpressure on the Top Flat Section.

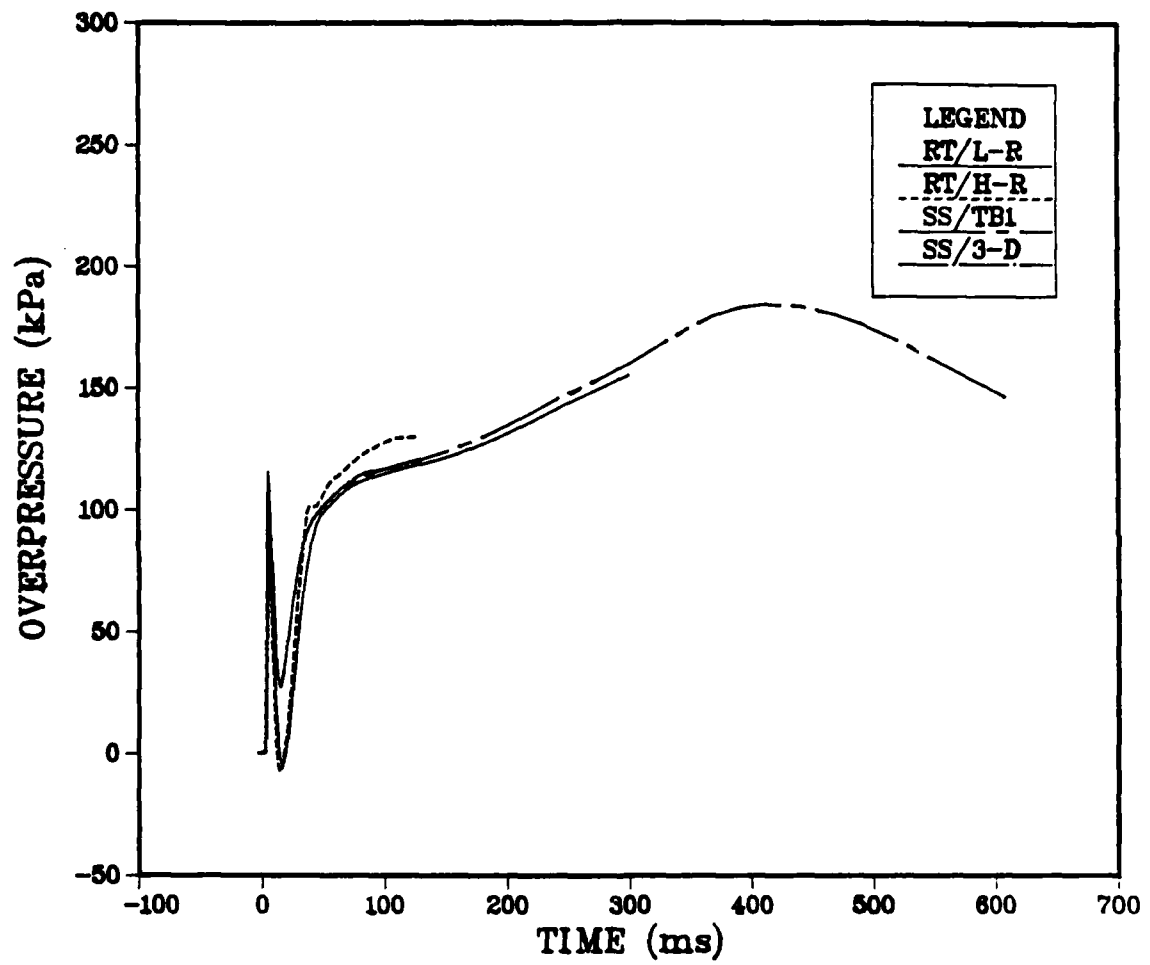


Figure 12. Comparison Computations for Average Overpressure on the Back Slope.

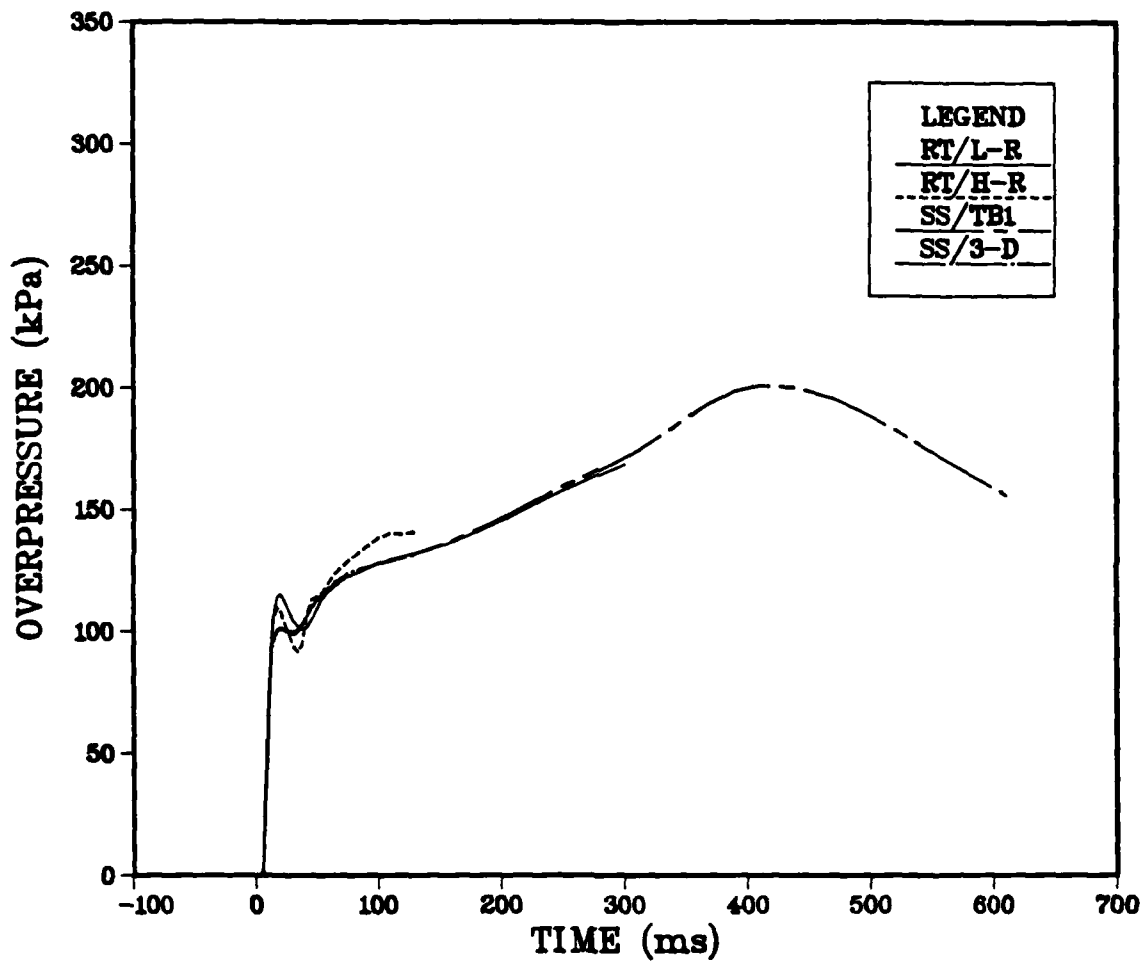


Figure 13. Comparison Computations for Average Overpressure on the Back Face.

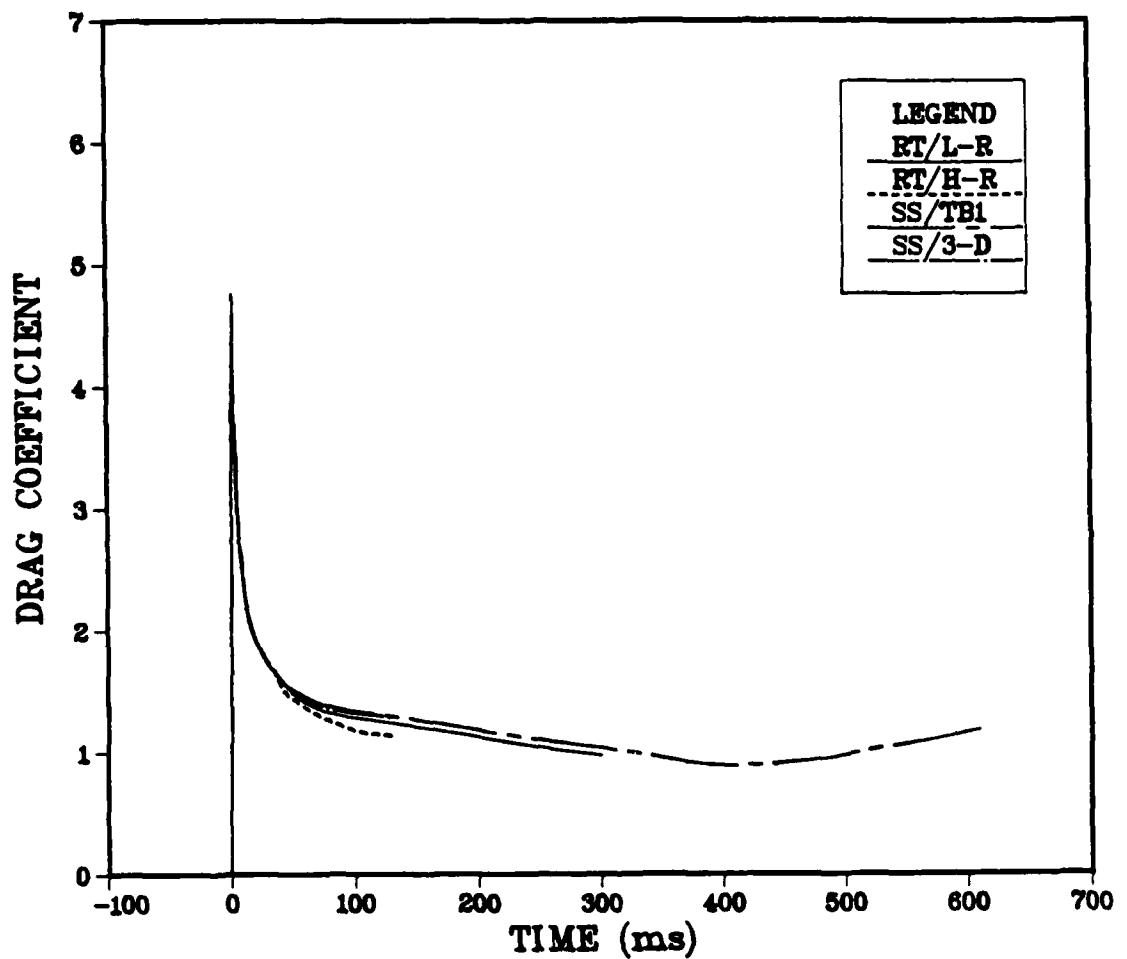


Figure 14. Comparison Computations for Drag Coefficient.

## V. CONCLUSION

The simple, zero-gradient, transmissive boundaries used in the HULL hydrocode cannot be expected to allow waves of any type to pass through them without reflecting an artificial wave of the same type back into the computational grid. The artificial reflected wave seems to have a strength that is directly proportional to the strength of the incoming wave. These boundaries are not self-correcting, because no solution is imposed on them. Thus, running a computation for an extended time will not assure the user that the boundaries will return to some "correct" state. These artificial disturbances propagate throughout the computational flow field. The velocities of these disturbances and their arrival times at regions of interest can be estimated using a relatively simple analytical technique based on geometry, incident shock velocity, and the shocked gas properties. Thus the results from this analysis can be used to identify which boundaries or regions of boundaries are likely to be the source of particular disturbances.

The analysis of the computations presented here was made more difficult by the improper modelling by HULL of the vortex that forms immediately downstream from the back face of this blunt 2-D target after the diffraction phase. As the computation progressed, the length of the "vortex" grew seemingly without bound in the downstream direction while maintaining a constant height roughly comparable to the height of the target. This generated an artificially strong reverse flow along the ground plane directed toward the back face of the target. This caused a large, additional artificial loading of the back of the target at a very early time, plus an increase in the vertical loading of the top flat section and back slope. Hence, the net effect of the overstated vortex was to produce an artificially increased hold-down force and an artificially decreased net horizontal force as the drag phase progressed, so the resistance of the target to translation and overturning is overstated. It is doubtful that the use of greater resolution in the flow field would do anything to make a fundamental improvement in the modelling of the vortex. At best, the artificial growth might be delayed, but probably not for long. The inability to dissipate such rotation is probably intrinsic to codes like HULL that solve the inviscid Euler equations for multidimensional flow in sets of one-dimensional steps using only pressure as the driving potential.

HULL is still an excellent code for free airblast and diffraction phase loading of both 2-D and 3-D targets: it is both fast-running and accurate. It also does well, considering that it is inviscid, for use in modelling late-time loading of simple 3-D and quasi-3-D targets because vortex growth in the downstream direction is inhibited by the transverse pressure gradients. Thus, back face loading does not have the same opportunity for artificial growth as it does in 2-D flow over a blunt target. Care must be taken to keep any transmissive boundaries remote from the region of interest.

## REFERENCES

1. J.A. Hasdal, B.S. Chambers, and R.W. Clemens, "Support to BRL: HULL Code Implementation on a CDC 7600," SAI-80-701-AQ, Science Applications, Inc., McLean, VA, August 1979.
2. B.S. Chambers, III, and J.D. Wortman, "Two-Dimensional Shore (Partial Island) Cells for BRL HULL," US Army Ballistic Research Laboratory Contract Report, ARBRL-CR-00497, Aberdeen Proving Ground, MD, December 1982 (AD A1234357).
3. R.E. Lottero, J.D. Wortman, B.P. Bertrand, and C.W. Kitchens, Jr., "Three-Dimensional Oblique Shock Diffraction over a Rectangular Parallelepiped: Computational/Experimental Comparison," US Army Ballistic Research Laboratory Technical Report ARBRL-TR-02443, Aberdeen Proving Ground, MD, November 1982. (AD 122254).
4. N.H. Ethridge, R.E. Lottero, J.D. Wortman, and B.P. Bertrand, "Flow Blockage and Its Effect on Minimum Incident Overpressure for Overturning Vehicles in a Large Blast Simulator," Proceedings of the Seventh International Symposium on Military Applications of Blast Simulation, Vol. II, Medicine Hat, Alberta, Canada, 13-17 July 1981.
5. J.D. Wortman. and R.E. Lottero, Comparison of HULL Hydrocode Computations of Shock Tube Blockage Effects on Target Loading for Step Shocks and Rapidly-Decaying Shocks," US Army Ballistic Research Laboratory Memorandum Report ARBRL-MR-03232, Aberdeen Proving Ground, MD, December 1982. (AD 123274).
6. N.H. Ethridge, R.E. Lottero, J.D. Wortman, and B.P. Bertrand, "Blockage Effects in a Large Blast Simulator," Proceedings of the Eighth International Symposium on Military Applications of Blast Simulation, Spiez, Switzerland, 20-24 June, 1983.
7. B.L. Tucker, "Transient Drag and American Machine Foundry Project MR-1013," Sandia Corporation Technical Memorandum 260-55-51, December 21, 1955.
8. Anon., "Transient Drag and Its Effect on Structures," Final Report, American Machine and Foundry Company, Project MR-1013, February 25, 1955.
9. S.F. Hoerner, "Fluid-Dynamic Drag," Published by S.F. Hoerner, 1965, Library of Congress Catalog Card Number 64-19666.
10. J.A. Schmitt, R.E. Lottero, and H.J. Goodman, "Analytic Model and Numerical Simulation of Shock Wave Propagation into a Reentrant Corner," US Army Ballistic Research Laboratory Technical Report ARBRL-TR-02286, Aberdeen Proving Ground, MD, January 1981 (AD A097471).

DISTRIBUTION LIST

<u>No. of Copies</u>	<u>Organization</u>	<u>No. of Copies</u>	<u>Organization</u>
12	Administrator Defense Technical Info Center ATTN: DTIC-DDA Cameron Station Alexandria, VA 22304-6145	1	Director Defense Communications Agency ATTN: 930 Washington, DC 20305
1	Director of Defense Research & Engineering ATTN: DD/TWP Washington, DC 20301	9	Director Defense Nuclear Agency ATTN: DDST TIPL/Tech Lib SPSS/K. Goering SPTD/T. Kennedy SPAS/P.R. Rohr G. Ullrich STSP/COL Kovel NATD NATA Washington, DC 20305
1	Asst. to the Secretary of Defense (Atomic Energy) ATTN: Document Control Washington, DC 20301		
1	Director Defense Advanced Research Projects Agency ATTN: Tech Lib 1400 Wilson Boulevard Arlington, VA 22209	2	Commander Field Command, DNA ATTN: FCPR FCTMOF Kirtland AFB, NM 87117
2	Director Federal Emergency Management Agency ATTN: D. A. Bettge Technical Library Washington, DC 20472	1	Commander Field Command, DNA Livermore Branch ATTN: FCPRL P.O. Box 808 Livermore, CA 94550
1	Director Defense Intelligence Agency ATTN: DT-2/Wpns & Sys Div Washington, DC 20301	1	HQDA DAMA-ART-M Washington, DC 20310
1	Director National Security Agency ATTN: E. F. Butala, R15 Ft. George G. Meade, MD 20755	10	Central Intelligence Agency Office of Central Reference Dissemination Branch Room GE-47 HQS Washington, DC 20502
1	Director Joint Strategic Target Planning Staff JCS Offut AFB Omaha, NB 68113	1	Program Manager US Army BMD Program Office ATTN: John Shea 5001 Eisenhower Avenue Alexandria, VA 22333

DISTRIBUTION LIST

<u>No. of Copies</u>	<u>Organization</u>	<u>No. of Copies</u>	<u>Organization</u>
2	Director US Army BMD Advanced Technology Center ATTN: CRDABH-X CRDABH-S Huntsville, AL 35807	1	US Army Belvoir R&D Center ATTN: STRBE-GE, D. Frink Fort Belvoir, VA 22060
1	Commander US Army BMD Command ATTN: BDMSC-TFN/N.J. Hurst P.O. Box 1500 Huntsville, AL 35807	1	Commander US Army Materiel Command ATTN: AMCDRA-ST 5001 Eisenhower Avenue Alexandria, VA 22333-0001
1	Commander US Army Engineer Division ATTN: HNDED-FD P.O. Box 1500 Huntsville, AL 35807	1	Commander Armament R&D Center US Army AMCCOM ATTN: SMCAR-TDC Dover, NJ 07801
2	Deputy Chief of Staff for Operations and Plans ATTN: Technical Library Director of Chemical & Nuc Operations Department of the Army Washington, DC 20310	2	Commander Armament R&D Center US Army AMCCOM ATTN: W. Reiner SMCAR-TSS Dover, NJ 07801
2	Office, Chief of Engineers Department of the Army ATTN: DAEN-MCE-D DAEN-RDM 890 South Pickett Street Alexandria, VA 22304	1	Commander US Army Armament, Munitions and Chemical Command ATTN: SMCAR-ESP-L Rock Island, IL 61299
3	Commander US Army Engineer Waterways Experiment Station ATTN: Technical Library Jim Watt Jim Ingram P.O. Box 631 Vicksburg, MS 39180	1	Director Benet Weapons Laboratory Armament R&D Center US Army AMCCOM ATTN: SMCAR-LCB-TL Watervliet, NY 12189
1	Commander US Army Engineering Center ATTN: ATSEN-SY-L Fort Belvoir, VA 22060	1	Commander US Army Aviation Research and Development Command ATTN: AMSAV-E 4300 Goodfellow Boulevard St. Louis, MO 63120
		1	Director US Army Air Mobility Research and Development Laboratory Ames Research Center Moffett Field, CA 94035

DISTRIBUTION LIST

<u>No. of Copies</u>	<u>Organization</u>	<u>No. of Copies</u>	<u>Organization</u>
1	Commander US Army Communications - Electronics Command ATTN: AMSEL-ED Fort Monmouth, NJ 07703	1	Commander US Army Missile Command Research, Development and Engineering Center ATTN: AMSMI-RD Redstone Arsenal, AL 35898
1	Commander US Army Communications Rsch and Development Command ATTN: DRSEL-ATDD Fort Monmouth, NJ 07703	1	Director US Army Missile and Space Intelligence Center ATTN: AIAMS-YDL Redstone Arsenal, AL 35898-5500
1	Commander ERADCOM Technical Library ATTN: DELSD-L (Reports Section) Fort Monmouth, NJ 07703-5301	2	Commander US Army Natick Research and Development Center ATTN: DRXRE/Dr. D. Sieling STRNC-UE/J. Calligeros Natick, MA 01762
2	Commander US Army Electronics Research and Development Command ATTN: DELEW-E, W. S. McAfee DELSD-EI, J. Roma Fort Monmouth, NJ 07703-5301	1	Commander US Army Tank Automotive Rsch and Development Command ATTN: AMSTA-TSL Warren, MI 48397-5000
7	Director US Army Harry Diamond Labs ATTN: Mr. James Gaul Mr. L. Belliveau Mr. J. Meszaros Mr. J. Gwaltney Mr. Bill Vault Mr. R. J. Bostak Dr. W. J. Schuman, Jr. 2800 Powder Mill Road Adelphi, MD 20783	1	Commander US Army Foreign Science and Technology Center ATTN: Rsch & Cncepts Br 220 7th Street, NE Charlottesville, VA 22901
4	Director US Army Harry Diamond Labs ATTN: DELHD-TA-L DRXDO-TI/002 DRXDO-NP DELHD-RBA/J. Rosado 800 Powder Mill Road Adelphi, MD 20783	1	Commander US Army Logistics Management Center ATTN: ATCL-O, Mr. Robert Cameron Fort Lee, VA 23801
		3	Commander US Army Materials Technology Laboratory ATTN: Technical Library DRXMR-ER, Joe Prifti Eugene de Luca Watertown, MA 02172

DISTRIBUTION LIST

<u>No. of Copies</u>	<u>Organization</u>	<u>No. of Copies</u>	<u>Organization</u>
1	Commander US Army Research Office P.O. Box 12211 Research Triangle Park NC 27709	1	Commandant Interservice Nuclear Weapons School ATTN: Technical Library Kirtland AFB, NM 87115
4	Commander US Army Nuclear & Chemical Agency ATTN: ACTA-NAW MONA-WE Technical Library LTC Finno 7500 Backlick Rd, Bldg. 2073 Springfield, VA 22150	1	Chief of Naval Material ATTN: MAT 0323 Department of the Navy Arlington, VA 22217
1	Commander US Army TRADOC ATTN: DCST&E Fort Monroe, VA 23651	2	Chief of Naval Operations ATTN: OP-03EG OP-985F Department of the Navy Washington, DC 20350
2	Director US Army TRADOC Systems Analysis Activity ATTN: LTC John Hesse ATAA-SL White Sands Missile Range NM 88002	1	Chief of Naval Research ATTN: N. Perrone Department of the Navy Arlington, VA 22217
1	Commander US Combined Arms Combat Developments Activity ATTN: ATCA-CO, Mr. L. C. Pleger Fort Leavenworth, KS 66027	1	Director Strategic Systems Projects Ofc ATTN: NSP-43, Tech Library Department of the Navy Washington, DC 20360
2	Commandant US Army Infantry School ATTN: ATSH-CD-CSO-OR Fort Benning, GA 31905	1	Commander Naval Electronic Systems Com ATTN: PME 117-21A Washington, DC 20360
1	Commander US Army Development & Employment Agency ATTN: MODE-TED-SAB Fort Lewis, WA 98433	1	Commander Naval Facilities Engineering Command Washington, DC 20360
		1	Commander Naval Sea Systems Command ATTN: SEA-62R Department of the Navy Washington, DC 20362

DISTRIBUTION LIST

<u>No. of Copies</u>	<u>Organization</u>	<u>No. of Copies</u>	<u>Organization</u>
3	Officer-in-Charge (Code L31) Civil Engineering Laboratory Naval Constr Bn Center ATTN: Stan Takahashi R. J. Odello Technical Library Port Hueneme, CA 93041	1	AFSC/SDOA Andrews Air Force Base MD 20334
1	Commander David W. Taylor Naval Ship Research & Development Ctr ATTN: Lib Div, Code 522 Bethesda, MD 20084	1	ADTC/DLODL, Tech Lib Eglin AFB, FL 32542
1	Commander Naval Surface Weapons Center ATTN: DX-21, Library Br. Dahlgren, VA 22448	1	AFWL/SUL Kirtland AFB, NM 87117
2	Commander Naval Surface Weapons Center ATTN: Code WA501/Navy Nuclear Programs Office Code WX21/Tech Library Silver Spring, MD 20910	1	Air Force Armament Laboratory ATTN: AFATL/DLODL Eglin AFB, FL 32542-5000
1	Commander Naval Weapons Center ATTN: Code 533, Tech Lib China Lake, CA 93555	1	AFATL (DLYV) Eglin AFB, FL 32542
1	Commander Naval Weapons Evaluation Fac ATTN: Document Control Kirtland AFB, NM 87117	1	RADC (EMTLD/Docu Library) Griffiss AFB, NY 13441
1	Commander Naval Weapons Center ATTN: Code 533, Tech Lib China Lake, CA 93555	1	AFWL/NTE, CPT J. Clifford Kirtland AFB, NM 87117
1	Commander Naval Weapons Evaluation Fac ATTN: Document Control Kirtland AFB, NM 87117	2	Commander-in-Chief Strategic Air Command ATTN: NRI-STINFO Lib Offutt AFB, NB 68113
1	Commander Naval Research Laboratory ATTN: Code 2027, Tech Lib Washington, DC 20375	1	AFIT (Lib Bldg. 640, Area B) Wright-Patterson AFB Ohio 45433
1	Superintendent Naval Postgraduate School ATTN: Code 2124, Technical Reports Library Monterey, CA 93940	1	FTD/NIIS Wright-Patterson AFB Ohio 45433
		1	Director Lawrence Livermore Lab. ATTN: Tech Info Dept L-3 P.O. Box 808 Livermore, CA 94550

DISTRIBUTION LIST

<u>No. of Copies</u>	<u>Organization</u>	<u>No. of Copies</u>	<u>Organization</u>
2	Director Los Alamos Scientific Lab. ATTN: Doc Control for Rpts Lib P.O. Box 1663 Los Alamos, NM 87544	1	Agbabian Associates ATTN: M. Agbabian 250 North Nash Street El Segundo, CA 90245
2	Director Sandia Laboratories ATTN: Doc Control for 3141 Sandia Rpt Collection L. J. Vortman P.O. Box 5800 Albuquerque, NM 87185	1	The BDM Corporation ATTN: Richard Hensley P.O. Box 9274 Albuquerque International Albuquerque, NM 87119
1	Director Sandia Laboratories Livermore Laboratory ATTN: Doc Control for Technical Library P.O. Box 969 Livermore, CA 94550	1	The Boeing Company ATTN: Aerospace Library P.O. Box 3707 Seattle, WA 98124
1	Director National Aeronautics and Space Administration Scientific & Tech Info Fac P.O. Box 8757 Baltimore/Washington International Airport MD 21240	2	California Research and Technology ATTN: M. Rosenblatt F. Sauer Suite B 130 11875 Dublin Blvd Dublin, CA 94568
1	Director NASA-Ames Research Center Applied Computational Aerodynamics Branch MS 202-14, Dr. T. Holtz Moffett Field, CA 94035	1	Carpenter Research Corporation ATTN: H. Jerry Carpenter Suite 424 904 Silver Spur Road Rolling Hills Estates, CA 90274
1	Aberdeen Research Center 30 Diamond Street Aberdeen, MD 21001	1	Goodyear Aerospace Corp ATTN: R. M. Brown, Bldg 1 Shelter Engineering Litchfield Park, AZ 85340
1	Aerospace Corporation ATTN: Tech Info Services P.O. Box 92957 Los Angeles, CA 90009	6	Kaman AviDyne ATTN: Dr. R. Reuteneck (4 cys) Mr. S. Criscione Mr. R. Milligan 83 Second Avenue Northwest Industrial Park Burlington, MA 01830

DISTRIBUTION LIST

<u>No. of Copies</u>	<u>Organization</u>	<u>No. of Copies</u>	<u>Organization</u>
3	Kaman Sciences Corporation ATTN: Library P. A. Ellis F. H. Shelton 1500 Garden of the Gods Road Colorado Springs, CO 80907	2	Physics International Corp 2700 Merced Street San Leandro, CA 94577
1	Kaman Sciences Corporation ATTN: Don Sachs Suite 703 2001 Jefferson Davis Highway Arlington, VA 22202	2	R&D Associates ATTN: Technical Library Allan Kuhl P.O. Box 9695 Marina del Rey, CA 90291
1	Kaman-TEMPO ATTN: DASIAC P.O. Drawer QQ Santa Barbara, CA 93102	2	Science Applications, Inc. ATTN: W. Layson John Cockayne PO BOX 1303 1710 Goodridge Drive McLean, VA 22102
1	Kaman-TEMPO ATTN: E. Bryant, Suite UL-1 715 Shamrock Road Bel Air, MD 21014	1	Science Applications, Inc. ATTN: Technical Library 1250 Prospect Plaza La Jolla, CA 92037
1	Lockheed Missiles & Space Co. ATTN: J. J. Murphy, Dept. 81-11, Bldg. 154 P.O. Box 504 Sunnyvale, CA 94086	2	Systems, Science and Software ATTN: C. E. Needham Lynn Kennedy PO Box 8243 Albuquerque, NM 87198
1	Martin Marietta Aerospace Orlando Division ATTN: G. Fotieo P.O. Box 5837 Orlando, FL 32805	3	Systems, Science and Software ATTN: Technical Library R. Duff K. Pyatt PO Box 1620 La Jolla, CA 92037
2	McDonnell Douglas Astronautics Corporation ATTN: Robert W. Halprin K.A. Heinly 5301 Bolsa Avenue Huntington Beach, CA 92647	1	Texas Engineering Experiment Station ATTN: Dr. D. Anderson 301 Engineering Research Center College Station, TX 77843
1	New Mexico Engineering Research Institute (CERF) ATTN: J. Leigh P.O. Box 25 UNM Albuquerque, NM 87131	2	TRW Systems Group ATTN: Benjamin Sussoltz Stanton Fink One Space Park Redondo Beach, CA 90278

DISTRIBUTION LIST

<u>No. of Copies</u>	<u>Organization</u>	<u>Aberdeen Proving Ground</u>
1	Battelle Memorial Institute ATTN: Technical Library 505 King Avenue Columbus, OH 43201	Dir, USAMSAA ATTN: AMXSY-D AMXSY-MP, H. Cohen
1	California Inst of Tech ATTN: T. J. Ahrens 1201 E. California Blvd. Pasadena, CA 91109	Cdr, USATECOM ATTN: AMSTE-TO-F
2	Denver Research Institute University of Denver ATTN: Mr. J. Wisotski Technical Library PO Box 10127 Denver, CO 80210	Cdr, CRDC, AMCCOM ATTN: SMCCR-RSP-A SMCCR-MU SMCCR-SPS-IL
1	TRW Ballistic Missile Division ATTN: H. Korman, Mail Station 526/614 P.O. Box 1310 San Bernadino, CA 92402	
1	Massachusetts Institute of Technology Aeroelastic and Structures Research Laboratory ATTN: Dr. E. A. Witmer Cambridge, MA 02139	
2	Southwest Research Institute ATTN: Dr. W. E. Baker A. B. Wenzel 8500 Culebra Road San Antonio, TX 78228	
1	SRI International ATTN: Dr. G. R. Abrahamson 333 Ravenswood Avenue Menlo Park, CA 94025	
1	Stanford University ATTN: Dr. D. Bershader Durand Laboratory Stanford, CA 94305	

### USER EVALUATION SHEET/CHANGE OF ADDRESS

This Laboratory undertakes a continuing effort to improve the quality of the reports it publishes. Your comments/answers to the items/questions below will aid us in our efforts.

1. BRL Report Number \_\_\_\_\_ Date of Report \_\_\_\_\_

2. Date Report Received \_\_\_\_\_

3. Does this report satisfy a need? (Comment on purpose, related project, or other area of interest for which the report will be used.)  
\_\_\_\_\_  
\_\_\_\_\_

4. How specifically, is the report being used? (Information source, design data, procedure, source of ideas, etc.)  
\_\_\_\_\_  
\_\_\_\_\_

5. Has the information in this report led to any quantitative savings as far as man-hours or dollars saved, operating costs avoided or efficiencies achieved, etc? If so, please elaborate.  
\_\_\_\_\_  
\_\_\_\_\_

6. General Comments. What do you think should be changed to improve future reports? (Indicate changes to organization, technical content, format, etc.)  
\_\_\_\_\_  
\_\_\_\_\_

Name \_\_\_\_\_

CURRENT  
ADDRESS      Organization \_\_\_\_\_

Address \_\_\_\_\_

City, State, Zip \_\_\_\_\_

7. If indicating a Change of Address or Address Correction, please provide the New or Correct Address in Block 6 above and the Old or Incorrect address below.

Name \_\_\_\_\_

OLD  
ADDRESS      Organization \_\_\_\_\_

Address \_\_\_\_\_

City, State, Zip \_\_\_\_\_

(Remove this sheet along the perforation, fold as indicated, staple or tape closed, and mail.)

— — — — — FOLD HERE — — — — —

Director  
U.S. Army Ballistic Research Laboratory  
ATTN: SLCBR-DD-T  
Aberdeen Proving Ground, MD 21005-5066

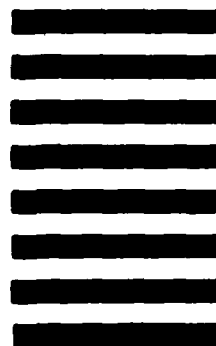


NO POSTAGE  
NECESSARY  
IF MAILED  
IN THE  
UNITED STATES

OFFICIAL BUSINESS  
PENALTY FOR PRIVATE USE. \$300

**BUSINESS REPLY MAIL**  
FIRST CLASS PERMIT NO 12062 WASHINGTON, DC  
POSTAGE WILL BE PAID BY DEPARTMENT OF THE ARMY

Director  
U.S. Army Ballistic Research Laboratory  
ATTN: SLCBR-DD-T  
Aberdeen Proving Ground, MD 21005-9989



— — — — — FOLD HERE — — — — —



FILMED

6-86

DTC